Relative Magnitude of Infragravity Waves at Coastal Dikes with Shallow Foreshores: A Prediction Tool

Christopher H. Lashley[1]; Jeremy D. Bricker[2,3]; Jentsje van der Meer, M.ASCE[4,5]; Corrado Altomare[6,7]; and Tomohiro Suzuki[8,9]

Abstract: Despite the widely recognized role of infragravity (IG) waves in many often-hazardous nearshore processes, spectral wave models, which exclude IG-wave dynamics, are often used in the design and assessment of coastal dikes. Consequently, the safety of these structures in environments where IG waves dominate remains uncertain. Here, we combine physical and numerical modeling to: (1) assess the influence of various offshore, foreshore, and dike slope conditions on the dominance of IG waves over those at sea and swell (SS) frequencies; and (2) develop a predictive model for the relative magnitude of IG waves, defined as the ratio of the IG-to-SS-wave height at the dike toe. Findings show that higher, directionally narrow-banded incident waves; shallower water depths; milder foreshore slopes; reduced vegetated cover; and milder dike slopes promote IG-wave dominance. In addition, the empirical model derived, which captures the combined effect of the varied environmental parameters, allows practitioners to quickly estimate the significance of IG waves at the coast, and may also be combined with spectral wave models to extend their applicability to areas where IG waves contribute significantly. **DOI: 10.1061/(ASCE)WW.1943-5460.0000576**. *This work is made available under the terms of the Creative Commons Attribution 4.0 International license, https://creativecommons.org/licenses/by/4.0/.*

Author keywords: Infragravity wave; Shallow foreshore; Vegetation; Combined physical and numerical modeling; XBeach; Predictive equation.

Introduction

Background

Infragravity (IG) waves, often referred to as "long," "surfbeat," or "tsunami-like" waves, are now widely recognized as the driving force behind several critical nearshore processes: beach and dune erosion (Roelvink et al. 2009), the development of seiches in harbors (Okihiro et al. 1993), and wave-driven coastal inundation

[1]Ph.D. Researcher, Dept. of Hydraulic Engineering, Delft Univ. of Technology, Stevinweg 1, 2628 CN Delft, Netherlands (corresponding author). ORCID: https://orcid.org/0000-0001-7149-2864. Email: c.h.lashley@tudelft.nl

[2]Associate Professor, Dept. of Hydraulic Engineering, Delft Univ. of Technology, Stevinweg 1, 2628 CN Delft, Netherlands. Email: j.d.bricker@tudelft.nl

[3]Visiting Associate Professor, Dept. of Civil and Environmental Engineering, Univ. of Michigan, 2350 Hayward St., Ann Arbor, MI 48109-2125.

[4]Principal, Van der Meer Consulting, P.O. Box 11, 8490 AA Akkrum, Netherlands. Email: jm@vandermeerconsulting.nl

[5]Professor, Water Science and Engineering Dept., IHE Delft, Westvest 7, 2611 AX Delft, Netherlands.

[6]Postdoctoral Researcher, Universitat Politecnica de Catalunya—BarcelonaTech, carrer Jordi Girona 1-3, 08034 Barcelona, Spain. Email: co.altomare@gmail.com

[7]Postdoctoral Researcher, Dept. of Civil Engineering, Ghent Univ., 9000 Ghent, Belgium.

[8]Senior Researcher, Flanders Hydraulics Research, Berchemlei 115, 2140 Antwerp, Belgium. ORCID: https://orcid.org/0000-0002-6008-4440. Email: tomohiro.suzuki@mow.vlaanderen.be

[9]Visiting Researcher, Dept. of Hydraulic Engineering, Delft Univ. of Technology, Stevinweg 1, 2628 CN Delft, Netherlands.

(Stockdon et al. 2006). Recent observations of the impact of IG waves include: unexpectedly high runup levels observed at the rocky coast of Banneg Island on the island of Simeulue off the coast of Sumatra (Sheremet et al. 2014); extensive damage and casualties that occurred along a coral reef-lined coast in the Philippines during Typhoon Haiyan (Roeber and Bricker 2015; Shimozono et al. 2015); and on the west coast of France, where several dunes were eroded and "over-washed" (Baumann et al. 2017; Lashley et al. 2019a). In each of these cases, the observed extreme water levels and resulting damage have been attributed to the presence or dominance of nearshore IG waves.

In deep water, these long-period, low-amplitude waves are formed through nonlinear interactions of sea and swell (hereafter sea–swell, SS) wave components (Longuet-Higgins and Stewart 1962), such as those locally generated by wind (sea), and those generated by distant storms (swell). The resulting wave-group pattern, with sequences of higher and lower amplitudes, generates an IG wave that travels bound to, and π radians out of phase with, the wave group.

As SS waves approach shallow, mildly sloping foreshores, they experience shoaling and continue to transfer energy to the bound IG wave, resulting in its amplitude growth. After SS waves break, the wave-group structure disappears and the bound IG wave is either freed (released) (Masselink 1995) or dissipates together with the SS waves (Baldock 2012). This enhancement and subsequent freeing of the bound IG wave is considered to be the main generation mechanism of nearshore IG waves on mild slopes ($\beta_b \leq 0.3$)], where the normalized bed-slope parameter (β_b) is defined as (Battjes et al. 2004)

$$\beta_b = \frac{\beta}{\omega}\sqrt{\frac{g}{h_b}} \tag{1}$$

where β = bed slope (taken here as foreshore slope, $\tan \alpha_{\text{fore}}$); the angular frequency of the IG wave, $\omega = 2\pi f_{\text{low}}$, where f_{low} = mean frequency of the IG wave at the breakpoint; and $h_b = H_{m0}/\Omega$ is

the mean breaker depth, where Ω = ratio of local wave height to water depth at the breakpoint.

Alternatively, nearshore IG waves may be generated on steep slopes ($\beta_b \geq 1$) by the temporal variation in the location of breaking waves. This occurs when alternating groups of higher- and lower-amplitude waves break farther and closer to the shore, respectively. The resulting fluctuations in wave setup and setdown, with the period of the wave groups, produce both seaward- and shoreward-propagating IG waves (Battjes et al. 2004; Symonds et al. 1982) which are out-of-phase and in-phase with the wave groups, respectively (Baldock et al. 2000).

These free IG waves are able to propagate in very shallow water where they either slowly dissipate by: (1) bottom friction (Henderson and Bowen 2002; Pomeroy et al. 2012), (2) IG-wave breaking (de Bakker et al. 2014; van Dongeren et al. 2007), (3) the nonlinear transfer of energy back to higher frequencies (Henderson et al. 2006), or are reflected off the coast or structure, forming (partially) standing waves (Sheremet et al. 2002). The magnitude of these IG waves at the shoreline can be substantial, exceeding that of waves at SS frequencies. Under these conditions of dominance, IG waves govern wave runup and, consequently, the potential for wave-induced flooding and coastal erosion (Guza and Thornton 1982; Holman and Sallenger 1985; Lashley et al. 2018; Ruessink et al. 1998; Ruggiero et al. 2004; van Gent 2001).

In the design and assessment of coastal dikes, the extent of wave runup and the associated volume of water that overtops the dike are typically assessed using empirical formulae that require wave height at the dike toe as input (Mase et al. 2013; van der Meer et al. 2018; van Gent 2001). Given their computational efficiency, spectral wave models, such as SWAN (Booij et al. 1999) and STWAVE (Smith et al. 2001), are now widely used to estimate wave conditions at the dike toe, including vegetation effects (Suzuki et al. 2012). While these phase-averaged models may accurately estimate the SS-wave height at the toe ($H_{m0,SS,toe}$), they exclude the nonlinear interactions that force the IG-wave component ($H_{m0,IG,toe}$) (Nwogu and Demirbilek 2010). Thus, their applicability to cases with shallow foreshores, where the ratio of local water depth at the dike toe to the offshore (deep-water) wave height, $h_{toe}/h_{m0,deep} < 4$ (Hofland et al. 2017), is limited; as IG waves tend to be significant under shallow conditions (Hofland et al. 2017; van Gent 2001). In light of this, it is the primary aim of the present paper to investigate the range of environmental conditions that promote the dominance of IG-wave energy at the toe of coastal dikes; and to provide a tool whereby the magnitude of $H_{m0,IG,toe}$, relative to $H_{m0,SS,toe}$, may be estimated as an indicator for the validity of these models.

Previous attempts have been made to relate the magnitude of IG-wave energy, either at the shore (in the form of swash) or near the shore, to parameters that describe the coastal environment; however, to date, the findings have been inconsistent. Guza and Thornton (1982) found that the IG component of wave runup increased linearly with increasing offshore wave height ($H_{m0,deep}$). Holman and Sallenger (1985) and Ruessink et al. (1998) later showed that it may be better predicted using the well-known breaker parameter (ξ_0), also referred to as the Iribarren number, which considers not only $H_{m0,deep}$ but also the deep-water wavelength (L_0) and α_{fore}. Contrastingly, Stockdon et al. (2006), in their analysis of six field sites, concluded that the IG component scaled better with $\sqrt{H_{m0,deep}L_0}$ and was actually independent of α_{fore}. For barred beaches, Cox et al. (2013) found a high correlation between shoreline IG motions and nearshore bar depth, suggesting that local water depth (h_{toe}), or local strong variations in foreshore geometry, plays a significant role. This finding also agrees well with studies on shallow reefs where wave characteristics were better described by relative water depth ($h_{toe}/H_{m0,deep}$), compared with

ξ_0 (Lashley et al. 2018; Yao et al. 2013). Diversely, Inch et al. (2017) found that nearshore IG waves were best predicted using an offshore forcing parameter that is proportional to the SS-wave energy flux $H_{m0,deep}^2 T_p$. More recently, both Gomes da Silva et al. (2018) and Passarella et al. (2018), in disagreement with Stockdon et al. (2006), argued that considering α_{fore} reduces IG-swash prediction errors. These contradictory findings both reveal that further research on the subject is required and suggest that nearshore IG-wave energy is unlikely a function of any single environmental factor.

Each of the aforementioned studies aimed at parameterizing IG-wave energy, at or near the shore, were limited to the environmental conditions of the geographic areas and time periods considered. Here, we combine the results of physical modeling and the XBeach phase-resolving numerical model (Smit et al. 2010) to generate a comprehensive dataset of varying (1) offshore forcing conditions (wave height, period, and directional spreading); (2) foreshore conditions (initial water depth, slope, vegetated cover, and bottom friction); and (3) dike slopes. XBeach, in nonhydrostatic mode, has been successfully used to reproduce nearshore hydrodynamics over a wide range of coastal environments under varying combinations of deep-water wave heights and periods; these include shallow, mildly sloping foreshores (Roelvink et al. 2018); shallow fringing reefs (Lashley et al. 2018; Pearson et al. 2017); vegetated coasts (van Rooijen et al. 2016); and steeply sloping gravel beaches (McCall et al. 2015). Therefore, the model is seen here as an appropriate tool to carry out the analysis.

Outline

This paper is an extension of work presented at the 29th International Ocean and Polar Engineering Conference (Lashley et al. 2019b), which was limited to the specific range of conditions of the physical experiment (described later "Physical Model Description") and considered only a single environmental parameter: initial water depth. In addition to an updated analysis, the current paper develops a predictive tool to quantify the importance of IG waves as a function of multiple environmental parameters. It is organized as follows: the "Methods" section provides descriptions of the numerical and physical models, followed by an overview of the formulae used to carry out the analyses. In the "Results and Discussions" section, XBeach is first validated and used, together with the physical experiment, to provide an in-depth discussion on the source of nearshore IG-wave energy; after which, the results of the numerical simulations of varied offshore, foreshore, and dike slope conditions are presented and discussed. This section ends by quantifying the influence of each parameter and providing an empirical model to predict the relative magnitude of nearshore IG waves. The "Conclusions" address the overall research objective and identifying areas for future work.

Methods

Physical Model Description

The physical modeling was performed at Flanders Hydraulics Research in a wave flume 70-m long, 4-m wide, and 1.45-m deep (Altomare et al. 2016). The experiments simulated the transformation of moderately steep spilling waves, with deep-water wave steepness, $s_0 \leq 0.26$ and $\xi_0 < 0.5$ (Table 1), over a smooth 1:50 sloping foreshore backed by a 1:2 sloping dike (Fig. 1) with varying offshore significant wave heights ($H_{m0,deep}$), spectral peak periods (T_p), and initial still-water depths (h_{toe}). The flume,

Table 1. Summary of physical model test conditions in both model and prototype scales, with the breaker parameter (ξ_0), relative water depth ($h_{\text{toe}}/H_{m0,\text{deep}}$), mean frequency of the IG wave at the breakpoint (f_{low}), normalized bed slope (β_b), and observed relative magnitude of infragravity waves ($\tilde{H}_{\text{IG}}$, Eq. 22) values

| | Model scale (1:25) | | | Prototype scale | | | | | | | |
Test No.	$H_{m0,\text{deep}}$ (m)	T_p (s)	h_{toe} (m)	$H_{m0,\text{deep}}$ (m)	T_p (s)	h_{toe} (m)	ξ_0	$H_{\text{toe}}/H_{m0,\text{deep}}$	f_{low} (Hz)	β_b	$\tilde{H}_{\text{IG}}$
1	0.067	2.30	0.030	1.675	11.50	0.757	0.22	0.452	0.06	0.50	1.05
2	0.057	2.53	0.001	1.425	12.65	0.025	0.26	0.018	0.06	0.53	1.43
3	0.085	2.32	0.001	2.125	11.60	0.020	0.20	0.009	0.05	0.47	1.74
4	0.100	2.32	0.001	2.500	11.60	0.025	0.18	0.010	0.05	0.48	1.82
5	0.121	2.30	0.001	3.025	11.50	0.025	0.17	0.008	0.05	0.42	2.01
6	0.068	2.28	0.050	1.700	11.40	1.250	0.22	0.735	0.07	0.41	0.85
7	0.059	2.48	0.050	1.475	12.40	1.262	0.26	0.856	0.06	0.48	0.70
8	0.065	2.28	0.050	1.625	11.40	1.250	0.22	0.769	0.06	0.48	0.82
9	0.114	2.31	0.050	2.850	11.55	1.250	0.17	0.439	0.05	0.41	1.20
10	0.115	2.53	0.050	2.875	12.65	1.250	0.19	0.435	0.05	0.42	1.12
11	0.060	2.29	0.031	1.500	11.45	0.787	0.23	0.525	0.06	0.49	0.96
12	0.052	2.48	0.002	1.300	12.40	0.050	0.27	0.038	0.06	0.55	1.39
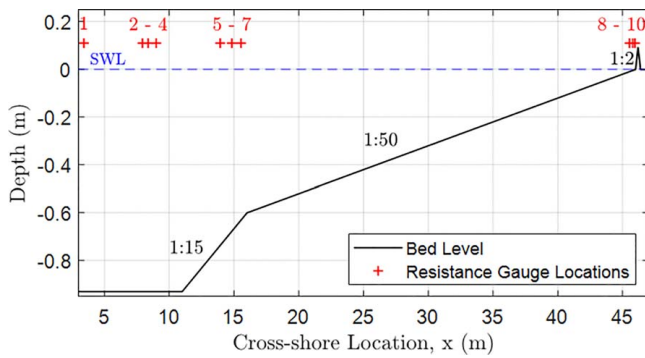
Fig. 1. Physical model setup showing resistance gauge locations. (Reprinted with permission from Lashley et al. 2019b.)

equipped with second-order wave generation, produced irregular waves that corresponded to a JONSWAP-type spectrum with a peak enhancement factor of 3.3 and a duration equal to 1,000 times T_p (~1,000 waves). The variations of water–surface elevations were measured using 10 resistance-type gauges, all synchronously sampling at 50 Hz (Fig. 1). Considering a geometric scaling of 1:25, conditions at the dike toe were measured 1 m (prototype scale) seaward of the dike base (at gauge 10). Table 1 provides a summary of the test conditions.

Numerical Model Description

Governing Equations
For this study, we applied the open-source XBeach numerical model. The nonhydrostatic mode (XB-NH) resolves both infragravity and sea–swell wave motions and is thus referred to as phase-resolving. It computes depth-averaged flow due to waves and currents using the nonlinear shallow water equations, including the effect of vegetation. The governing equations, in one-dimensional form, follow

$$\frac{\partial \eta}{\partial t} + \frac{\partial uh}{\partial x} = 0 \tag{2}$$

$$\frac{\partial u}{\partial t} + u\frac{\partial u}{\partial x} - v_h\frac{\partial^2 u}{\partial x^2} = -\frac{1}{\rho}\frac{\partial(\bar{q} + \rho g\eta)}{\partial x} - c_f\frac{u|u|}{h} + \frac{F_v}{\rho h} \tag{3}$$

where x and t = horizontal spatial and temporal coordinates, respectively; η = free surface elevation; u = depth-averaged cross-shore velocity; v_h = horizontal eddy viscosity (Smagorinsky 1963); h = water depth; ρ = density of water; c_f = bed friction factor; and

F_v = depth-averaged vegetation force (van Rooijen et al. 2016). The depth-averaged dynamic (nonhydrostatic) pressure normalized by the density, $\bar{q}$, is computed from the mean of the dynamic pressure at the surface (q_s, assumed to be zero) and the bed (q_b, by assuming a linear change over depth). In order to compute the dynamic pressure at the bed, the contributions of advective and diffusive terms to the vertical momentum balance are considered negligible:

$$\frac{\partial w}{\partial t} + \frac{\partial q}{\partial z} = 0 \tag{4}$$

where w = vertical velocity; and z = vertical coordinate. The vertical velocity at the bed is set by the kinematic boundary condition

$$w_b = u\frac{\partial(\eta - h)}{\partial x} \tag{5}$$

and the vertical momentum balance at the surface follows

$$\frac{\partial w_s}{\partial t} = 2\frac{q_b}{h} - \frac{\partial w_b}{\partial t} \tag{6}$$

The dynamic pressure at the bed is then solved by combining Eq. (6) and the local continuity equation:

$$\frac{\partial u}{\partial x} + \frac{w_s - w_b}{h} = 0 \tag{7}$$

In the present study, we obtain c_f from the Manning's roughness coefficient (n) as (Roelvink et al. 2015)

$$c_f = \frac{n^2 g}{\sqrt[3]{h}} \tag{8}$$

F_v is obtained by integrating the drag force per unit height (F_D) over the vegetation height (a_h) (Dalrymple et al. 1984):

$$F_D = \frac{1}{2}\rho C_D b_v N_v\, u|u| \tag{9}$$

where C_D = drag coefficient; b_v = vegetation stem diameter; and N_v = vegetation density. Though not assessed as part of the present study, the performance of XBeach in simulating the effects of vegetation has been previously validated with data from two physical experiments, showing high skill (van Rooijen et al. 2016). Note that a recent study using SWASH reveals that the effects of porosity and inertia of vegetation can be important for wave propagation in dense vegetation fields (Suzuki et al. 2019). However, those effects were not taken into consideration in this study since the vegetation considered here is not so dense to have a significant influence on the results.

To control the computed location and magnitude of depth-limited wave breaking, a hydrostatic front approximation is applied. The pressure distribution under breaking waves is therefore considered to be hydrostatic once the local surface steepness exceeds a maximum value (Smit et al. 2010). This criterion is controlled by the user-specified *maxbrsteep* parameter.

Model Setup
The numerical simulations were first configured using a 1D approach to represent actual flume conditions. In the current study, we apply the configuration of Lashley et al. (2018) that obtained reasonably accurate results when applied to similar shallow environments (fringing reefs). As such, the maximum breaking wave steepness (*maxbrsteep*) was set to 0.5, compared with its default value of 0.6; and n was set to 0.012 s/m$^{1/3}$ to represent a relatively smooth flume bottom (Suzuki et al. 2017). The cross-shore grid spacing (Δx) applied varied from a maximum of $L_0/100$ (offshore) to a minimum of 1 m (dike toe). This choice of varying Δx minimized computation time while ensuring that the waves were accurately resolved. No further tuning of the model was done as part of this study.

For validation, the model was forced at its boundary with time series of velocities derived from the paddle motion observed during the physical experiment, which corresponded to a JONSWAP-type spectrum and included the generation of second-order bound waves. Likewise, the extent of numerical model domain corresponded to that of the physical flume (Fig. 1).

While assessing the influence of the varied environmental parameters (described in "Environmental Parameters for Numerical Simulations"), the model domain was allowed to vary depending on the water depth and foreshore slope (Fig. 2). These simulations were forced with irregular waves generated using parametric (JONSWAP-type) spectra with a peak enhancement factor of 3.3. For the numerical simulations where directional spreading was considered, a 2DH approach was adopted with cyclic lateral boundaries. This approach assumed alongshore uniformity and used an alongshore grid spacing, $\Delta y = 2\Delta x$, which was found to be optimal considering both accuracy and computational demand. All other model parameters were set to match the 1D simulations.

It should be noted that the numerical model, like the physical experiments, assumes bound IG waves at its boundary and does not consider potentially free IG waves arriving at the boundary from distant sources. Likewise, neither the physical experiment nor the 1D numerical simulations contain (2D) trapped IG waves, which might have an effect in the field. They do, however, consider the generation of free IG waves resulting from the shoaling and breaking of the SS-wave groups within the model domain.
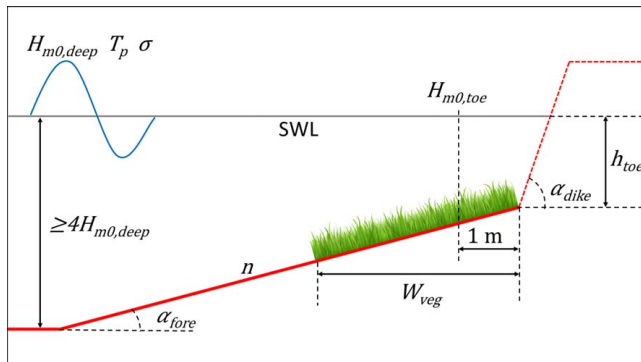

Fig. 2. Schematic representation of dike–foreshore system indicating the relevant environmental parameters.

Validation Metrics
In order to assess the performance of XB-NH, we applied the following objective functions: Scatter Index (SCI), as a normalized measure of error [Eq. (10)]; and Relative Bias (Rel.bias), as an indicator of prediction bias [Eq. (11)]:

$$\text{SCI}_{\Psi} = \frac{\sqrt{\frac{1}{n}\sum_{i=1}^{N}(\Psi_{\text{XB}}^i - \Psi_{\text{Obs}}^i)^2}}{\frac{1}{n}\sum_{i=1}^{N}\Psi_{\text{Obs}}^i} \tag{10}$$

and

$$\text{Rel.bias}_{\Psi} = \frac{\sum_{i=1}^{N}(\Psi_{\text{XB}}^i - \Psi_{\text{Obs}}^i)}{\sum_{i=1}^{N}\Psi_{\text{Obs}}^i} \tag{11}$$

where Ψ = the parameter being evaluated, in a sample size N; and subscripts XB and Obs = XBeach predictions and observations during the physical experiment, respectively. Lower SCI values (<0.15) indicate accurate model predictions (Roelvink et al. 2018), while a positive or negative Rel.bias estimate indicates a systematic over- or under-prediction, correspondingly.

Data Processing and Analysis

Mean Water Level
The mean water level ($\bar{\eta}$) was calculated by taking the mean of the surface elevation time series, $\eta(t)$ at each instrument location, relative to the base of the dike (unless otherwise stated).

Separation of Sea–Swell and Infragravity Waves
The time series of $\eta(t)$ were further analyzed using the Welch's average periodogram method and a Hann filter with a 50% maximum overlap. The resulting 1D spectra of wave-energy density, $C_{\eta\eta}(f)$, with $\sim$43° of freedom (Percival and Walden 1993) and a frequency resolution of $\sim$0.008 Hz, were then used to determine the significant wave heights in both the SS ($H_{m0,\text{SS}}$) and IG ($H_{m0,\text{IG}}$) bands, as

$$H_{m0,\text{SS}} = 4\sqrt{\int_{f_p/2}^{1} C_{\eta\eta}df} \tag{12}$$

and

$$H_{m0,\text{IG}} = 4\sqrt{\int_{0.005}^{f_p/2} C_{\eta\eta}df} \tag{13}$$

where half the peak frequency ($f_p/2 = 1/2T_p$) is taken as the cutoff to separate SS and IG motions (Roelvink and Stive 1989). This choice of cutoff frequency is based on the tendency that, in deep water, the majority of SS-wave energy is found at frequencies $>f_p/2$, and the majority of IG-wave energy lies at frequencies $<f_p/2$.

Infragravity Wave-Generation Mechanisms
To investigate the generation of IG waves by either: (1) shoaling of the bound wave; or (2) breakpoint forcing, a cross-correlation analysis was carried out between the envelope of the SS waves, $A(t)$, and the low-pass filtered ($<f_p/2$) surface elevation time series, $\eta^{\text{IG}}(t)$, which represents IG motions. Following Janssen et al. (2003), $A(t)$ was calculated as

$$A(t) = |\eta^{\text{SS}}(t) + i\Gamma\{\eta^{\text{SS}}(t)\}|^{\text{IG}} \tag{14}$$

where $\eta^{\text{SS}}(t)$ = the high-pass filtered ($>f_p/2$) surface elevation time series, which represents SS motions; and Γ = the Hilbert transform operator.

The correlation between $A(t)$ (offshore) and $\eta^{\mathrm{IG}}(t)$ was then determined using the following cross-correlation function:

$$R_{\eta A} = \frac{\left\langle \eta^{\mathrm{IG}}(t) A(t + \tau) \right\rangle}{\sigma_\eta \sigma_A} \qquad (15)$$

where $\langle \ldots \rangle$ = a time averaging operator; τ = a time shift; and σ_η and σ_A = the standard deviations of $\eta^{\mathrm{IG}}(t)$ and $A(t)$, respectively; and $-1 \leq R_{\eta A} \leq 1$.

This approach has been found to successfully identify both bound incoming (negative $R_{\eta A}$) and outgoing free IG waves (positive/negative $R_{\eta A}$) (e.g., Janssen et al. 2003; List 1992); incoming breakpoint-generated IG waves (positive $R_{\eta A}$); and outgoing breakpoint-generated IG waves (negative $R_{\eta A}$) (e.g., Baldock and Huntley 2002; Pomeroy et al. 2012).

Separation of Incoming and Outgoing Infragravity Waves
The total low-pass filtered surface elevation signal was then separated into incoming, $\eta_{\mathrm{in}}(t)$, and outgoing, $\eta_{\mathrm{out}}(t)$, components as (Guza et al. 1984)

$$\eta^{\mathrm{IG}}(t) = \eta_{\mathrm{in}}^{\mathrm{IG}}(t) + \eta_{\mathrm{out}}^{\mathrm{IG}}(t) \qquad (16)$$

$$\eta_{\mathrm{in}}^{\mathrm{IG}}(t) = \frac{\eta^{\mathrm{IG}}(t) \cdot c_{\mathrm{in}} + u^{\mathrm{IG}}(t) \cdot h}{c_{\mathrm{in}} + c_{\mathrm{out}}} \qquad (17)$$

and

$$\eta_{\mathrm{out}}^{\mathrm{IG}}(t) = \frac{\eta^{\mathrm{IG}}(t) \cdot c_{\mathrm{out}} - u^{\mathrm{IG}}(t) \cdot h}{c_{\mathrm{in}} + c_{\mathrm{out}}} \qquad (18)$$

where

$$c_{\mathrm{in}} = \begin{cases} c_g & x < x_b \\ \sqrt{gh} & x \geq x_b \end{cases} \qquad (19)$$

$$c_{\mathrm{out}} = \sqrt{gh} \qquad (20)$$

where h = water depth at the location (including wave-induced setup); and $u(t)$ = horizontal velocity time series. Here, the incoming waves seaward of the breakpoint (x_b) are assumed to be bound, propagating with celerity (c) equal to the group velocity (c_g); while those shoreward of the breakpoint and those outgoing are assumed to be free waves traveling with $\sqrt{gh}$. This method, initially developed for normally incident, shallow-water (long) waves, requires colocated pressure gauges and current meters (to obtain $\eta(t)$ and $u(t)$, respectively) in order to decompose the total signal into seaward (outgoing) and shoreward (incoming) propagating components (Guza et al. 1984). These signals were then used to calculate the incoming and outgoing significant wave heights in the IG frequency bands ($H_{m0,\mathrm{IG,in}}$ and $H_{m0,\mathrm{IG,out}}$) using Eq. (13).

Identification of Standing Wave
Inshore of the forcing zone (shoreward of the breakpoint), the superposition of the incoming wave and that reflected at the structure form a standing-wave (List 1992). This standing wave is then characterized by areas of maximum energy (antinodes), where the total energy is approximately the sum of the incoming and outgoing waves, and areas of minimum energy (nodes), where the total energy is approximately equal to the difference between the incoming and outgoing waves.

For a given cross-shore location (x), the frequencies at which nodes in a standing wave occur were identified as (Buckley et al.

2018; Nwogu and Demirbilek 2010)

$$f_{\mathrm{node}} = \frac{1}{4}(2m - 1)\left(\int_x^{x_{\mathrm{dike}}} \frac{1}{\sqrt{gh}} dx \right)^{-1} \qquad (21)$$

where x_{dike} = the dike location (point of reflection); and m = number of nodes from the reflection point, and ($m = 1$ corresponds the fundamental mode of the dike–foreshore system. This equation considers the dike–foreshore system to be an open-ended basin of variable depth. It is based on the formation of a node at a distance from the structure equal to one-quarter the wavelength of a wave propagating with speed, $c = \sqrt{gh}$. By calculating this wave speed at discrete points across the foreshore, f_{node} may be obtained for the sloping bathymetry (Roeber and Bricker 2015).

Relative Magnitude of Infragravity Waves
We defined the relative magnitude of nearshore IG waves ($\tilde{H}_{\mathrm{IG}}$) as the ratio of $H_{m0,\mathrm{IG}}$ to $H_{m0,\mathrm{SS}}$ at the toe of the structure

$$\tilde{H}_{\mathrm{IG}} = \frac{H_{m0,\mathrm{IG,toe}}}{H_{m0,\mathrm{SS,toe}}} \qquad (22)$$

and IG-wave dominance where $\tilde{H}_{\mathrm{IG}} > 1$.

Environmental Parameters for Numerical Simulations

Following validation, XBeach was used to simulate a range of environmental parameters, specifically those related to hydrodynamic forcing conditions: (1) $H_{m0,\mathrm{deep}}$, T_p, and directional spreading width (σ); (2) foreshore conditions: h_{toe}, foreshore slope angle (α_{fore}), width of vegetated cover (W_{veg}), and bottom friction (n); (3) and dike slope angle (α_{dike}).

Selection Criteria for Parameter Values
The range of each parameter was selected to extend the analysis as far as possible while adhering to the limits of both nature and the reliability of the numerical model. The criteria applied to the selection of parameter values follow:
- $0.005 < s_0 < 0.05$ at the model boundary, where s_0 is the deep-water wave steepness
- The water depth at the model boundary $\geq 4H_{m0,\mathrm{deep}}$ to ensure that no depth-induced breaking occurred offshore (Hofland et al. 2017)
- $kh \leq 1$ at the model boundary to minimize the relative dispersion and celerity errors associated with the nonlinear shallow water equations, where wave number, $k = 2\pi/L$
- σ values of 0°, 10°, and 24° to represent wave flume, swell, and wind–sea conditions, respectively (Roelvink et al. 2018). This parameter may also be characterized by the user-defined spreading factor s in XBeach as

$$\sigma = \frac{180}{\pi} \sqrt{\frac{2}{s + 1}} \qquad (23)$$

- W_{veg}, measured as horizontal distance from the dike, ranged from 0 to 800 m, which is typical of salt marshes found in the Netherlands (Vuik, et al. 2016). A summary of the parameter values simulated is provided in Table 2 and the properties of the vegetation considered in Table 3; and
- n values of 0.012, 0.02, and 0.03 s/m$^{1/3}$ to represent smooth wave flume, muddy foreshore, and sandy foreshore conditions, respectively. This parameter is then converted to a dimensionless friction coefficient (c_f) in XBeach (Equation 8).

Following a one-[factor]-at-a-time (OAT) approach, each environmental parameter was varied one at a time, while all others remained constant. For example, in the assessment of the influence of

Table 2. Summary of values (prototype scale) for offshore significant wave height ($H_{m0,\text{deep}}$), peak period (T_p), directional spreading (σ), initial water depth (h_{toe}), foreshore slope ($\cot \alpha_{\text{fore}}$), width of vegetated cover (W_{veg}), bottom friction (n), and dike slope ($\cot \alpha_{\text{dike}}$)

$H_{m0,\text{deep}}$ (m)	T_p (s)	σ (°)	h_{toe} (m)	$\cot \alpha_{\text{fore}}$	W_{veg} (m)	n (s/m$^{1/3}$)	$\cot \alpha_{\text{dike}}$
1	5	0	0.5	10	0	0.012	2
3	6	10	1.0	25	200	0.020	4
5	7	24	1.5	50	400	0.030	6
7	8		2.0	100	600		10
9	9		2.5	250	800		∞^a
11	11		3.0	500			
	13		3.5	1,000			
	15		5.0				
	17						

[a]No-dike scenario.

Table 3. Vegetation properties representative of salt marshes in the Netherlands

Parameter	Value
Drag coefficient, C_D	0.4
Stem diameter, b_v	0.003 m
Density, N_v	1,200 stems/m^2
Height, a_h	0.3 m

Source: Data from Vuik et al. (2016).

initial water depth, h_{toe} was varied from 0 to 5 m, while σ, $\cot \alpha_{\text{fore}}$, W_{veg}, n, and $\cot \alpha_{\text{dike}}$ were kept constant at their reference values. For each parameter value, 24 combinations of $H_{m0,\text{deep}}$ and T_p ($0.005 < s_0 < 0.036$), based on Table 2 and the above criteria, were simulated at the model boundary. As a result, a total of 672 XBeach simulations were carried out.

Quantifying the Influence of Environmental Parameters

Influence factors [$\bar{\gamma}$, Eq. (24)], which describe the effect of each environmental parameter on $\tilde{H}_{\text{IG}}$, were obtained by analyzing the mean response of $\tilde{H}_{\text{IG}}$ to variations in each environmental parameter, relative to a reference case, where $h_{\text{toe}} = 1$ m, $\sigma = 1°$, $\cot \alpha_{\text{fore}} = 50$, $W_{\text{veg}} = 0$ m, $n = 0.012$ s/m$^{1/3}$, and $\cot \alpha_{\text{dike}} = 2$, for the 24 different combinations of $H_{m0,\text{deep}}$ and T_p:

$$\bar{\gamma}_\psi = \frac{1}{24} \sum_{i=1}^{24} \frac{\tilde{H}_{\text{IG},i}}{\tilde{H}_{\text{IG,ref},i}} \tag{24}$$

where the subscript ψ = the environmental parameter being evaluated; and subscript ref = the simulation with reference parameter values.

Results and Discussions

XBeach Validation

Before using XB-NH to generate the synthetic dataset, we first verify that it accurately simulates the hydrodynamics of shallow foreshore environments by comparing it to the observations of the physical experiment. The mean water levels ($\bar{\eta}$) predicted by XB-NH compare well with those observed during the physical experiment (Fig. 3), with minor SCI (0.069) and Rel.bias (0.053) error values. In particular, the location and magnitude of wave-induced setup (the rise in $\bar{\eta}$), shoreward of the breakpoint, where $h_b = H_{m0}/\Omega$, is well represented [Fig. 4(a)]. Here,
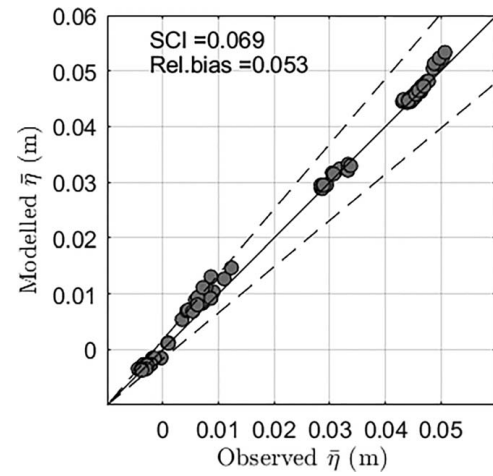

Fig. 3. Modeled and observed comparison of $\bar{\eta}$ (model scale).
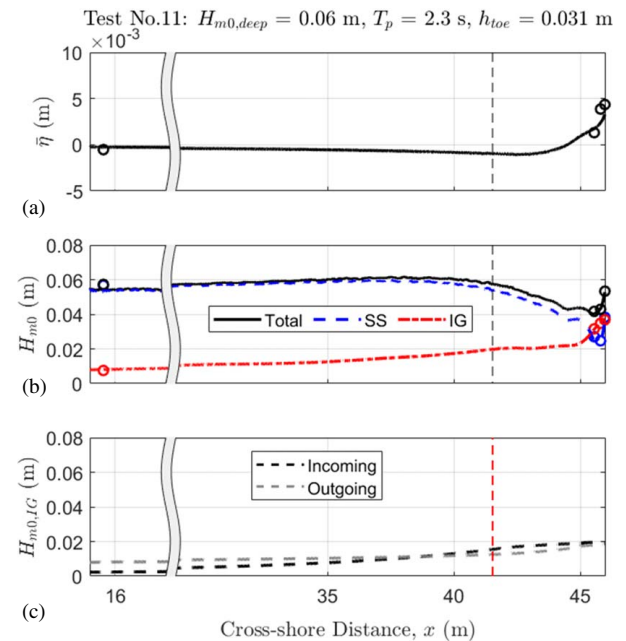

Fig. 4. Cross-shore profiles of modeled (lines) and observed (circles): (a) $\bar{\eta}$; (b) H_{m0}, showing the total, SS and IG signals; and (c) modeled incoming and outgoing $H_{m0,\text{IG}}$, for Test No. 11 (model scale). Dashed vertical lines indicate mean breakpoint.

the ratio of breaking waves to local water depth (Ω) is taken as 0.5; this value was found to best represent the onset of wave breaking [Fig. 4(b)].

Likewise, Fig. 4(b) shows good agreement between the modeled and observed $H_{m0,\text{IG}}$ and $H_{m0,\text{SS}}$. This cross-shore profile shows the growth of $H_{m0,\text{SS}}$ during shoaling (seaward of the breakpoint) and its subsequent dissipation by depth-induced breaking. Conversely, $H_{m0,\text{IG}}$ is enhanced during shoaling but continues to grow as SS waves break, resulting in IG-wave dominance at the dike toe. This is further seen in the transformation of wave spectra; Fig. 5 shows that XB-NH accurately captures the shift in spectral density, $C_{\eta\eta}(f)$ from SS to IG frequencies. This apparent transfer of energy to lower frequencies is due to the dissipation of SS waves by depth-induced breaking and the concurrent enhancement of IG waves. It should be noted that the results here differ from those
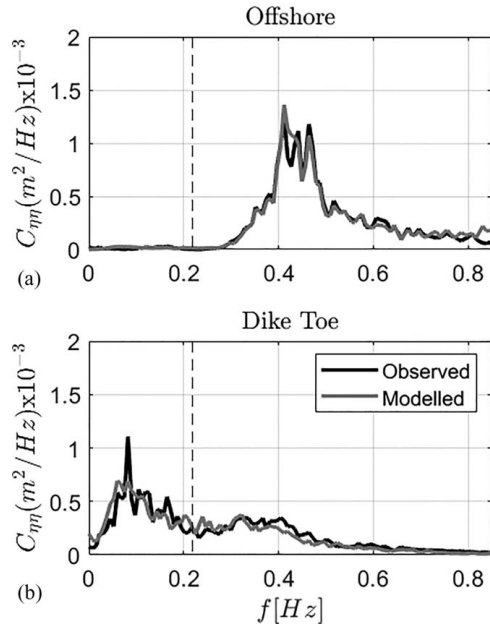
Fig. 5. Comparison of modeled and observed wave spectra: (a) offshore, at gauge 1; and (b) at the dike toe, at gauge 10, for Test No. 11 (model scale). Dashed lines represent the frequency separating SS and IG motions.

in Lashley et al. (2019b), as the observed surface elevation time series are used here as model input and not parametric spectra, for increased accuracy.

Considering the validation metrics, both $H_{m0,IG}$ and $H_{m0,SS}$ show little bias (Rel.bias values of 0.021 and −0.01, respectively); while $H_{m0,IG}$ predictions, though still considered accurate [SCI = 0.111, Fig. 6(a)], show more scatter than predictions of $H_{m0,SS}$ [SCI = 0.04, Fig. 6(b)]. That said, note that this difference in scatter is related to the low values of $H_{m0,IG}$ observed. The SCI is defined as the root-mean-square error (RMSE) between the model and observations, normalized by the mean of the observations [Eq. (10)]. Both predictions of $H_{m0,IG}$ and $H_{m0,SS}$ have similar RMSE values: 0.002 and 0.003 m, respectively; however, the lower mean of the observed $H_{m0,IG}$ results in a larger SCI value. Nevertheless, both SCI values are considered to be well within acceptable values: SCI < 0.15 or within 15% error (Roelvink et al. 2018).

To investigate the sensitivity of the predicted $\bar{\eta}$, $H_{m0,IG}$, and $H_{m0,SS}$ to the random wave components imposed at the model boundary, each XBeach simulation was run ten times with a new random-wave time series. However, the effects were found to be negligible (<3% variation in $H_{m0,IG}$ and <1% in both $\bar{\eta}$ and $H_{m0,SS}$).

Reflection of Infragravity Waves at the Dike

Fig. 4(c) shows the cross-shore evolution of the total incoming and outgoing $H_{m0,IG}$ for Test No. 11. The incoming IG waves gain energy over the shallow foreshore as SS waves shoal ($x > 28$ m) and break ($x \geq 41.5$ m), before finally experiencing near-complete reflection at the dike [$x = 46$ m, Fig. 4(c)]. The superposition of the incoming and the reflected outgoing IG signals results in a maximum total signal at the dike [Fig. 4(b)]. Following reflection, the outgoing waves experience inverse shoaling, also referred to as deshoaling (Battjes et al. 2004), where they reduce in amplitude with increasing water depth, that is as the wave celerity increases [Fig. 4(c)].
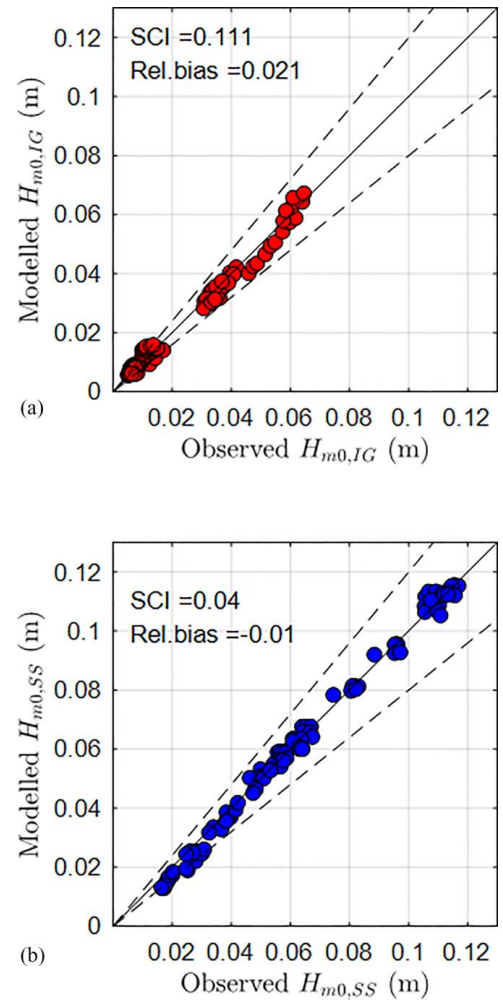

Fig. 6. Modeled and observed comparison of: (a) $H_{m0,IG}$; and (b) $H_{m0,SS}$ (model scale).

To investigate the presence of a standing wave, we analyze the evolution of wave spectral density at each cross-shore location, resulting in the spatial plot shown in Fig. 7. This was done first considering only the incoming signal [Fig. 7(a)], obtained by running the simulation without the dike, to exclude the effects of reflection, and then for the total signal where reflection from the dike is included [Fig. 7(b)]. A pattern of curved spectral ridges and troughs is clearly visible at low frequencies in Fig. 7(b) but absent in Fig. 7(a). These locations of minimum and maximum $C_{\eta\eta}(f)$ correspond to nodes and antinodes in a standing wave (Buckley et al. 2018; Klopman and van der Meer 1999; Symonds et al. 1982). This is further corroborated using Eq. (21), as the predicted f_{node} line corresponds well with the minima in $C_{\eta\eta}(f)$.

Infragravity Wave-Generation Mechanism

The high spatial resolution of the numerical model allows the presentation of the sequence of cross-correlations ($R_{\eta A}$) between the modeled local $\eta^{IG}(t)$ and $A(t)$ offshore ($x = 0$ m), at each cross-shore location, as a continuous spatial plot with ridges of positive and negative correlations (Fig. 8). The slight negative correlation seen at zero time lag ($\tau = 0$ s) corresponds to the trough of a bound IG wave that is out of phase with the incident wave groups (Longuet-Higgins and Stewart 1962).
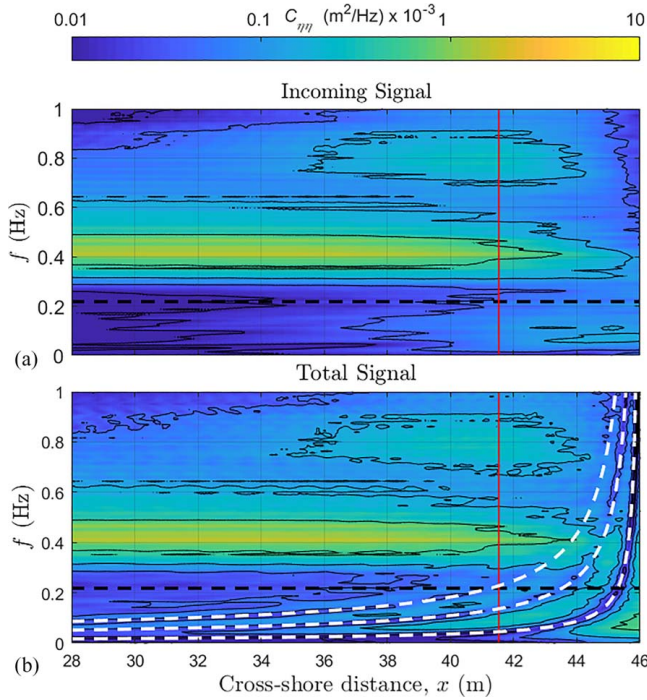
Fig. 7. Spatial evolution of wave spectral density for Test No. 11 based on: (a) the incoming; and (b) the total surface elevation signals. Dashed white curves show the predicted standing wave nodes [f_{node}, Eq. (21) for $m = 1, 2$ and 3]. Dashed black line shows cutoff frequency separating SS and IG motions. Vertical line indicates breakpoint location.

Fig. 8. Cross-correlation functions ($R_{\eta A}$) between $A(t)$ at $x = 0$ and $\eta^{\text{IG}}(t)$ at all cross-shore locations, as modeled in XBeach, for Test No.11 both: (a) with; (b) without the dike. Dashed black lines correspond to an incoming wave group propagating with celerity, c_g; dashed black-and-white lines represent an outgoing wave propagating with celerity $\sqrt{gh}$. Dashed vertical lines indicate the breakpoint; and (c) the bed level, for reference.

At $x \sim 10$ m, both this negative signal and a bar of positive correlation, which represents the crest of the bound wave, becomes more visible. Shoreward of this point ($x > 10$ m), the positive/negative form of the cross-correlation becomes stronger; this is consistent with an incident bound wave developing an asymmetric form during shoaling (Baldock and Huntley 2002; List 1992). Concurrently, the lag between the wave group, travelling with velocity (c_g), based on *linear wave theory* [black dashed line in Fig. 8(a and b)], and the trough of the bound wave increases. This phase shift allows the transfer of energy between the wave group and the bound wave, resulting in IG wave growth (van Dongeren and Svendsen 1997).

Shoreward of the breakpoint ($x_b = 41.5$ m), the ridge of positive correlation is strongly enhanced, suggesting the contribution of an incoming breakpoint-generated IG wave. The now-enhanced IG wave is reflected at the dike ($x = 46$ m, $\tau \sim 23$ s) and propagates to the offshore boundary ($x = 0$ m, $\tau \sim 53$ s) as a free long wave; that is, a wave propagating with celerity equal to $\sqrt{gh}$ [dashed black-and-white line in Fig. 8(a and b)].

Theoretically, breakpoint forcing would result in both incoming and outgoing IG waves propagating away from the breakpoint. However, this is not immediately evident in Fig. 8(a), as the outgoing signal is dominated by that reflected at the dike. To investigate this further, the simulation was rerun with the dike removed and the landward boundary set to absorbing–generating (weakly reflective). In the absence of a reflective boundary, a negatively correlated ridge may be seen extending from the breakpoint ($x_b = 41.5$ m, $\tau \sim 30$ s) to offshore ($x = 0$ m, $\tau \sim 49$ s) [Fig. 8(b)]. This negative cross-correlation corresponds to a seaward propagating free IG-wave generated by SS-wave breaking (Baldock 2006; Contardo and Symonds 2013; Pomeroy et al. 2012). Thus, the incoming IG waves shoreward of the breakpoint [$x > 41.5$ m, Fig. 8(a)] are the combined result of enhanced bound waves and
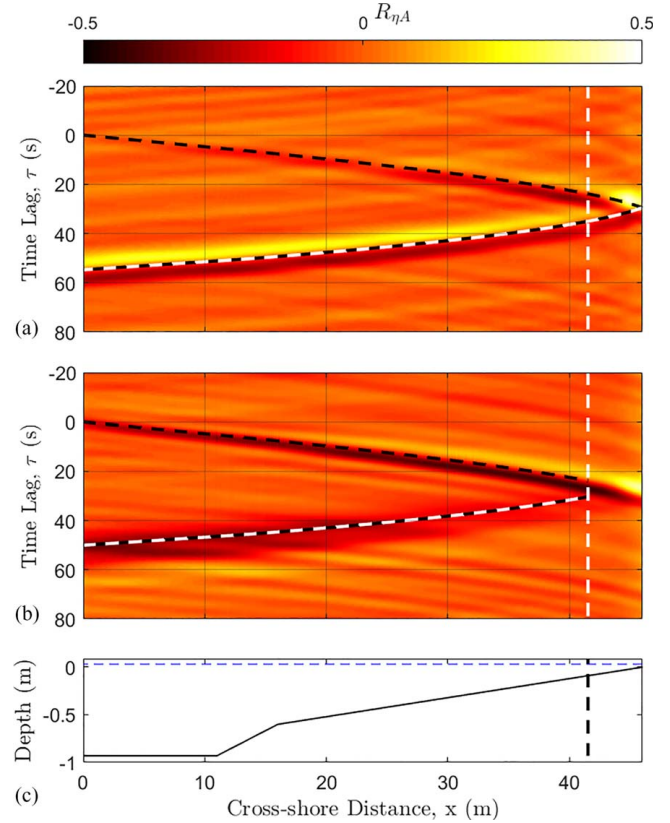
the shoreward propagating component of breakpoint forced waves. Accordingly, the IG waves propagating seaward (outgoing) are the combined result of the wave reflected at the dike and the wave radiated seaward directly from the breakpoint.

This finding is further supported by the normalized bed-slope parameter analysis where β_b ranged from 0.41 to 0.55 for the 12 physical model tests (Table 1). These values are over the threshold for bound-wave shoaling as the main generation mechanism ($\beta_b \leq 0.3$) but still under the threshold for breakpoint forcing to dominate ($\beta_b \geq 1$). This suggests that both generation mechanisms do indeed contribute to $H_{m0,\text{IG,toe}}$.

Influence of Environmental Parameters

Deep-Water Significant Wave Height and Peak Period

Given that $H_{m0,\text{deep}}$ and T_p are known to be correlated, we jointly assess their influence on nearshore wave conditions. Fig. 9 shows the variation in $H_{m0,\text{IG,toe}}$, $H_{m0,\text{SS,toe}}$, and $\tilde{H}_{\text{IG}}$ with changes in $H_{m0,\text{deep}}$ and T_P at the offshore boundary, while all other parameters were held constant: $h_{\text{toe}} = 1$ m, $\sigma = 0°$, $\cot \alpha_{\text{fore}} = 50$, $W_{\text{veg}} = 0$ m, $n = 0.012$ s/m$^{1/3}$, and $\cot \alpha_{\text{dike}} = \infty$. Both $H_{m0,\text{IG,toe}}$ [Fig. 9(a)] and $H_{m0,\text{SS,toe}}$ [Fig. 9(b)] increase linearly with increasing $H_{m0,\text{deep}}$ and, to a much lesser extent, T_p, made evident by the minimal scatter displayed. Likewise, Fig. 9(c) displays a clear positive relationship between $H_{m0,\text{deep}}$ and $\tilde{H}_{\text{IG}}$, with minor scatter associated with variations in T_p. This relationship is well described (coefficient of determination, $R^2 = 0.94$) by the following expression, obtained
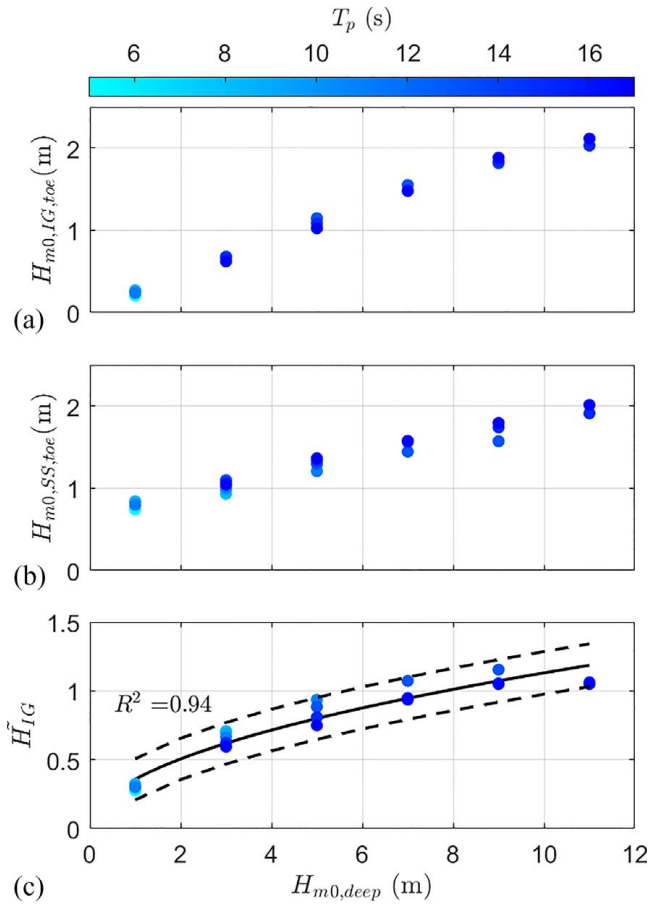
Fig. 9. Scatterplots of: (a) $H_{m0,IG,toe}$; (b) $H_{m0,SS,toe}$; and (c) $\tilde{H}_{IG}$ against $H_{m0,deep}$ under reference conditions ($\sigma = 0°$, $h_{toe} = 1$ m, cot $\alpha_{fore} = 50$, $W_{veg} = 0$ m, $n = 0.012$ s/m$^{1/3}$, and cot $\alpha_{dike} = \infty$), for each of the 24 combinations of $H_{m0,deep}$ and T_p simulated. Solid black line indicates model fit; dashed black lines indicate $\pm 95\%$ confidence intervals.

Fig. 10. Scatterplots of $\tilde{H}_{IG}$ against: (a) s_0; (b) $\sqrt{H_{m0,deep}L_0}$; and (c) $H_{m0,deep}^2 T_p$ under reference conditions ($\sigma = 0°$, $h_{toe} = 1$ m, cot $\alpha_{fore} = 50$, $W_{veg} = 0$ m, $n = 0.012$ s/m$^{1/3}$, and cot $\alpha_{dike} = \infty$), for each of the 24 combinations of $H_{m0,deep}$ and T_p simulated.

using the linear least-squares method:

$$\tilde{H}_{IG} = a \cdot H_{m0,deep}^{0.5} \tag{25}$$

where the fitted coefficient $a = 0.358$ (0.344, 0.371) m^{-1} for the previous reference parameter values; numbers in parentheses indicate the lower and upper 95% confidence bounds, respectively.

The strong dependence of both $H_{m0,IG,toe}$ and $H_{m0,SS,toe}$ on $H_{m0,deep}$ indicates an unsaturated surf zone, typical of steeper fore-shore slopes (Power et al. 2010; Stockdon et al. 2006), where the inner surf zone wave heights are equally dependent on the local water depth (h_{toe}) and the offshore wave height ($H_{m0,deep}$). This dependence also justifies the relationship obtained between $\tilde{H}_{IG}$ and $H_{m0,deep}$ [Eq. (25)]; that is, $\tilde{H}_{IG}$ exhibits a negative exponential (or negative power) relationship with $h_{toe}/H_{m0,deep}$, as shown in Lashley et al. (2019b), and hence a positive power relationship with $H_{m0,deep}/h_{toe}$. This ratio of offshore wave height to local water depth has been found to accurately describe both the intensity (Hofland et al. 2017; Lashley et al. 2018) and location of wave breaking (Yao et al. 2013), which in turn determine the magnitude of nearshore waves. Thus, for the constant water depth simulated here, ($h_{toe} = 1$ m), the power law holds. The influence of variations in h_{toe} is assessed, separately, in "Initial Water Depth at the Dike Toe."

We also assessed the influence of additional parameters that combine $H_{m0,deep}$ and T_p: s_0 [Fig. 10(a)]; $\sqrt{H_{m0,deep}L_0}$ [Fig. 10(b)], as
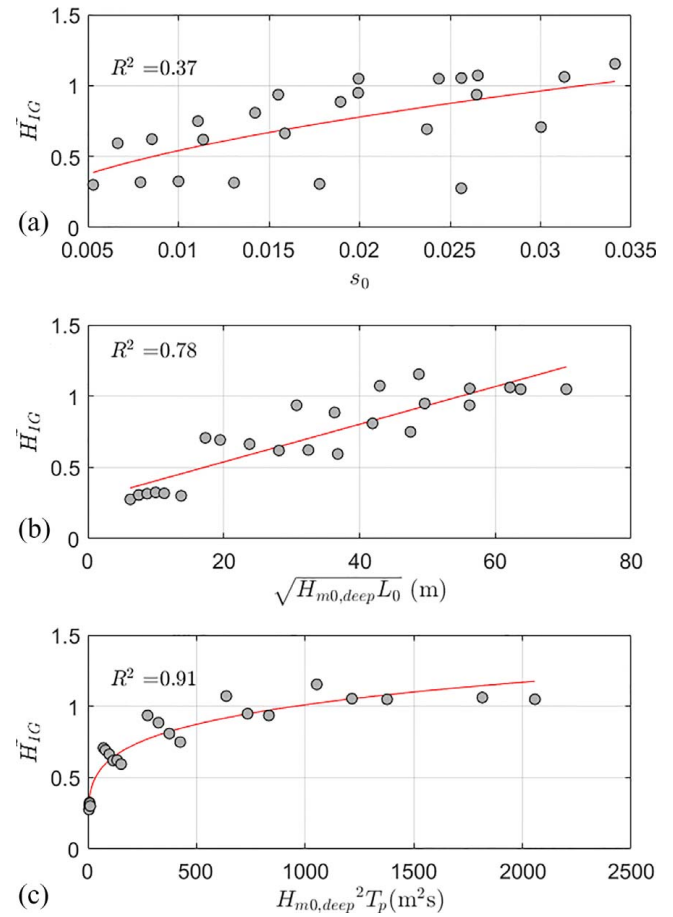
recommended by Stockdon et al. (2006), and $H_{m0,deep}^2 T_p$ [Fig. 10(c)], as proposed by Inch et al. (2017). However, while these parameters may describe the individual components ($H_{m0,IG,toe}$ and $H_{m0,SS,toe}$) well, as shown in their respective studies, they yielded lower R^2 values here, compared with Eq. (25). This suggests that T_p has only a minor influence on $\tilde{H}_{IG}$.

Deep-Water Directional Spreading

Considering wave flume ($\sigma = 0°$), typical swell ($\sigma = 10°$), and typical wind–sea ($\sigma = 24°$) conditions, a total of 72 estimates of $H_{m0,IG,toe}$ and $H_{m0,SS,toe}$ were obtained. Both parameters show negative relationships with σ (Fig. 11). However, $H_{m0,IG,toe}$ experiences 2.6 times more dissipation (on average) than does $H_{m0,SS,toe}$ for the same increase in σ, suggesting that wave energy at IG frequencies is significantly more sensitive to variations in σ. A change in σ from wave flume conditions to a typical wind–sea results in a 36% reduction in $H_{m0,IG,toe}$ compared with an 16% reduction in $H_{m0,SS,toe}$. This finding emphasizes the need to consider directional spreading in the offshore forcing, as the assumption of unidirectionality leads to unrealistically high estimates of $H_{m0,IG,toe}$ (van Dongeren et al. 2003). As $H_{m0,IG,toe}$ is more sensitive to changes in σ than $H_{m0,SS,toe}$, $\bar{\gamma}_\sigma$ decreases linearly with increasing σ (Fig. 12):

$$\bar{\gamma}_\sigma = 1 - 0.01 \cdot \sigma \tag{26}$$

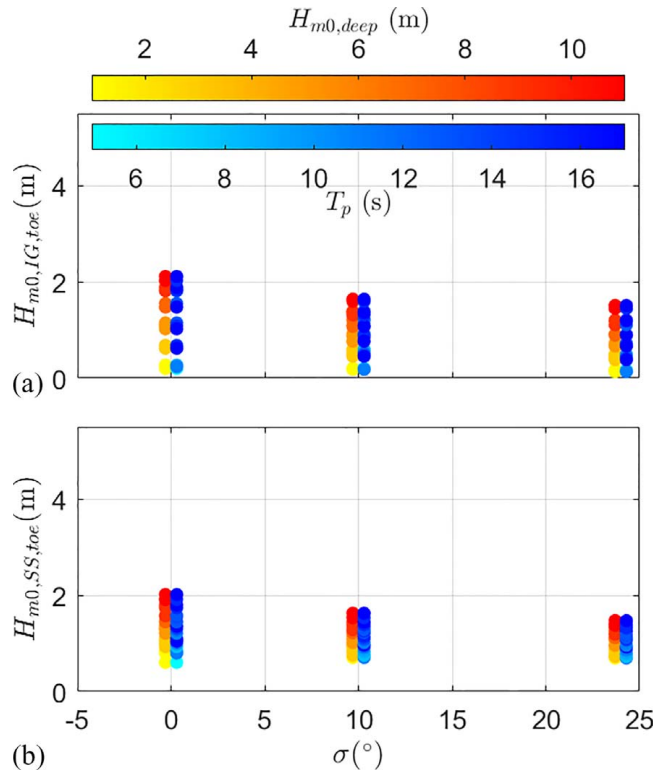where $\bar{\gamma}_\sigma = 1$ corresponds to the reference case.

Fig. 11. Scatterplots of: (a) $H_{m0,IG,toe}$; and (b) $H_{m0,SS,toe}$ against σ ($h_{toe} = 1$ m, cot $\alpha_{fore} = 50$, $W_{veg} = 0$ m, $n = 0.012$ s/m$^{1/3}$, and cot $\alpha_{dike} = \infty$). Each data point is represented by two markers with colormaps indicating the magnitude of $H_{m0,deep}$ (hot) and T_p (cold).
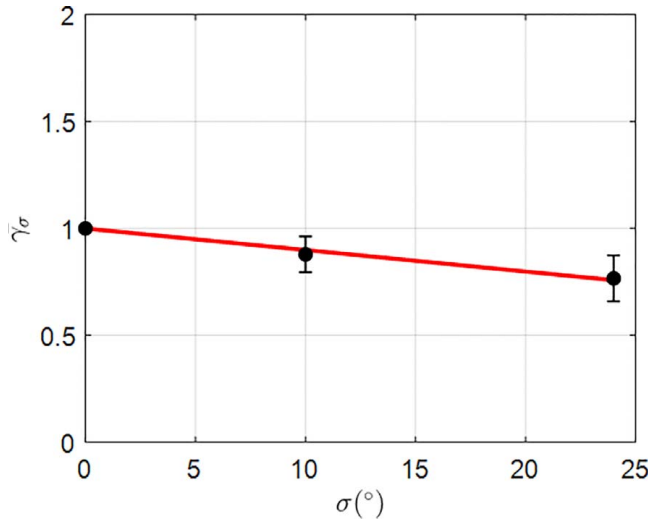

Fig. 12. Mean response of $\tilde{H}_{IG}$ to variations in σ, relative to the reference case ($\sigma = 0°$). Line indicates the model fit [Eq. (26)]. Vertical error bars represent the standard deviation of each mean.

Initial Water Depth at the Dike Toe

Each of the ten values of h_{toe} simulated (Table 2) was exposed to the 24 different combinations of $H_{m0,deep}$ and T_p, resulting in 240 estimates of $H_{m0,IG,toe}$ [Fig. 13(a)] and $H_{m0,SS,toe}$ [Fig. 13(b)] for analysis. In addition to the influence of h_{toe}, the combined influence, if any, of $H_{m0,deep}$ or T_p may be observed in the colormaps presented in Fig. 13.

Both $H_{m0,IG,toe}$ and $H_{m0,SS,toe}$ appear to decrease as the initial water depth becomes shallower (Fig. 13); however, this reduction
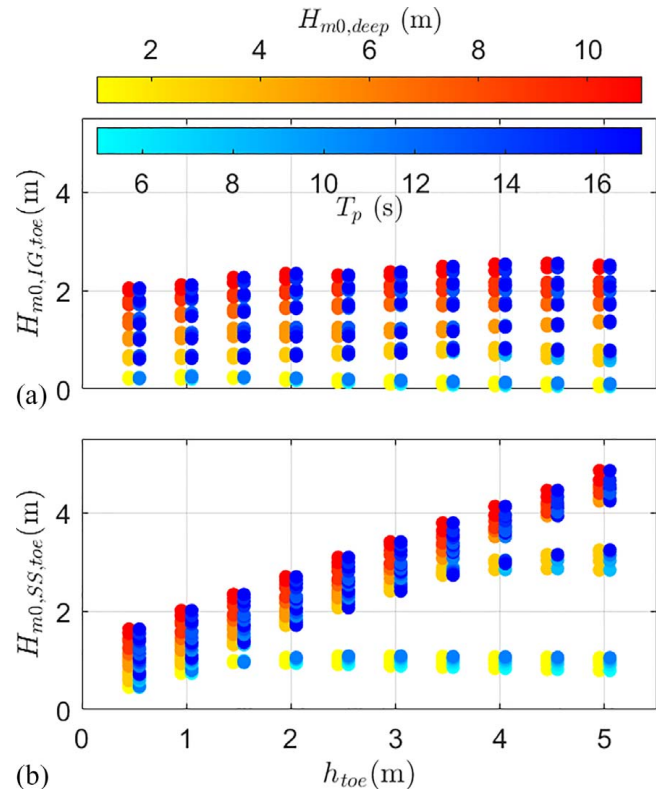
Fig. 13. Scatterplots of: (a) $H_{m0,IG,toe}$; and (b) $H_{m0,SS,toe}$ against h_{toe} ($\sigma = 0°$, cot $\alpha_{fore} = 50$, $W_{veg} = 0$ m, $n = 0.012$ s/m$^{1/3}$, and cot $\alpha_{dike} = \infty$). Each data point is represented by two markers with colormaps indicating the magnitude of $H_{m0,deep}$ (hot) and T_p (cold).

is more notable in $H_{m0,SS,toe}$, where a clear linear trend is observed. The points in Fig. 13(b) which appear to deviate from the general trend, at $h_{toe} = 1.5$ m and $h_{toe} = 3.5$ m, correspond to simulations with $H_{m0,deep} = 1$ m and $H_{m0,deep} = 3$ m, respectively. In these simulations, the relative water depth, $h_{toe}/H_{m0,deep} > 1.0$ and $H_{m0,SS,toe}$ is not yet depth limited.

To quantify the influence of h_{toe}, we analyze the average response of $\tilde{H}_{IG}$ to variations in h_{toe}, relative to that obtained for the reference case [$\bar{\gamma}_h$, Eq. (24)], where $h_{toe} = 1$ m. Fig. 14 shows that $\bar{\gamma}_h$, and thus $\tilde{H}_{IG}$, on average, increases exponentially with decreasing water depth. This observation is in agreement with the findings of Hofland et al. (2017), which showed that the spectral wave period ($T_{m-1,0}$) at the dike toe, which also represents the relative contribution of lower-frequency (IG) waves, increased exponentially with shallower water depths. By fitting a curve to the data, we obtain the following expression for the influence of h_{toe}:

$$\bar{\gamma}_h = 1.04 \cdot e^{-1.4 \cdot h_{toe}} + 0.9 \cdot e^{-0.19 \cdot h_{toe}} \qquad (27)$$

where $\bar{\gamma}_h = 1$ corresponds to the reference case.

Influence of Foreshore Slope

$H_{m0,IG,toe}$ initially increases as cot α_{fore} increases, reaching a maximum value at cot $\alpha_{fore} = 50$ [Fig. 15(a)]. This is due to the combination of both the bound-IG wave shoaling and breakpoint-generation mechanisms ($0.3 < \beta_b < 1$), as described in "Infragravity Wave-Generation Mechanism." However, as the foreshore becomes milder, as cot α_{fore} increases further, $H_{m0,IG,toe}$ decreases exponentially (note the log scale of the x-axis). On the other hand, $H_{m0,SS,toe}$ shows a consistent negative exponential relationship
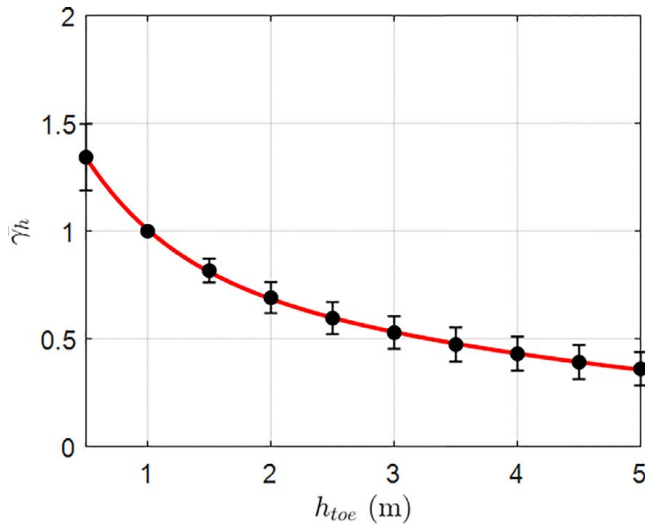
Fig. 14. Mean response of $\tilde{H}_{IG}$ to variations in h_{toe}, relative to the reference case ($h_{toe} = 1$ m). Line indicates the model fit [Eq. (27)]. Vertical error bars represent the standard deviation of each mean.
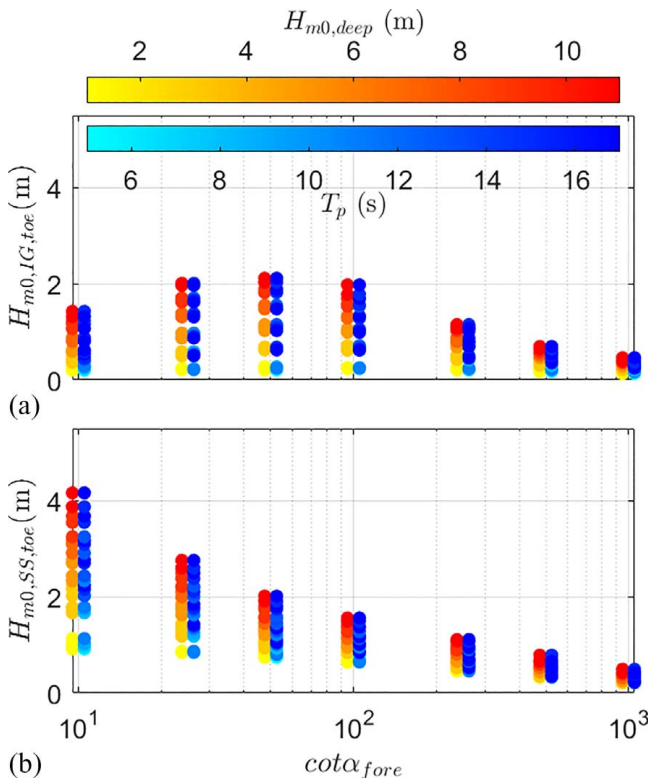

Fig. 15. Scatterplots of: (a) $H_{m0,IG,toe}$; and (b) $H_{m0,SS,toe}$ against cot α_{fore} ($\sigma = 0°$, $h_{toe} = 1$ m, $W_{veg} = 0$ m, $n = 0.012$ s/m$^{1/3}$, and cot $\alpha_{dike} = \infty$). Each data point is represented by two markers with colormaps indicating the magnitude of $H_{m0,deep}$ (hot) and T_p (cold).

with cot α_{fore} [Fig. 15(b)]. As SS waves begin to break further offshore with increasing cot α_{fore}, the surf zone becomes wider and results in increased dissipation.

These trends lend support to the arguments of Lara et al. (2011) and Baldock (2012) that suggest that the bound IG wave may not be released during SS-wave breaking, but remains locked and therefore dissipates in the surf zone concurrently with the SS waves that force it. This dissipation is less evident for steeper

slopes [Figs. 16(a and b)], as the bound wave may indeed experience some dissipation, but breakpoint forcing is strong inside the relatively narrow surf zone, thus leading to higher values of $H_{m0,IG,toe}$. However, as the foreshore becomes milder (cot $\alpha_{fore} > 100$; $\beta_b < 0.3$) and the surf zone wider, breakpoint forcing becomes weak, since its forcing (breaking) region becomes large in comparison to the wave-group motion (Baldock and Huntley 2002). This absence of breakpoint forcing and the dissipation of the bound IG wave in the surf zone results in lower values of $H_{m0,IG,toe}$ [Fig. 16(c)].

The mean response of $\tilde{H}_{IG}$ to variations in cot α_{fore}, relative to the reference case [$\bar{\gamma}_f$, Eq. (28)], shows three distinct trends (Fig. 17), dependent on the characteristics of wave breaking (represented here by cot α_{fore} and the relative water depth, $h_{toe}/H_{m0,deep}$). For steeper slopes (cot $\alpha_{fore} < 100$), $\bar{\gamma}_f$ increases logarithmically with increasing values of cot α_{fore} (red line in Fig. 17). This growth continues for milder slopes (cot $\alpha_{fore} > 100$) when $h_{toe}/H_{m0,deep} \geq 0.2$; however, for lower values of $h_{toe}/H_{m0,deep}$, the surf zone becomes very wide and $\bar{\gamma}_f$ decreases (blue line in Fig. 17). The relatively large variation in $\bar{\gamma}_f$ (magenta line) for cot $\alpha_{fore} = 500$ and cot $\alpha_{fore} = 1,000$, shown by the length of the error bars, is due to the increased influence of T_p on the breakpoint location and the overall surf zone width for very mild slopes.

$$\bar{\gamma}_f = \begin{cases} 1.56 - 3.09 \cdot \cot\alpha_{fore}^{-0.44} & \cot\alpha_{fore} \leq 100 \\ 0.51 \cdot \cot\alpha_{fore}^{0.18} & \cot\alpha_{fore} > 100, \ h_{toe}/H_{m0} \geq 0.2 \\ 1.62 \cdot \cot\alpha_{fore}^{-0.08} & \cot\alpha_{fore} > 100, \ h_{toe}/H_{m0} < 0.2 \end{cases} \tag{28}$$

where $\bar{\gamma}_f = 1$ corresponds to the reference case (cot $\alpha_{fore} = 50$).

In addition, we examined how $\tilde{H}_{IG}$ relates to the well-known normalized bed slope parameter (β_b), proposed by Battjes et al. (2004). In Fig. 18(a), $\tilde{H}_{IG}$ shows a negative exponential relationship with β_b; with scatter further highlighting the influence of $h_{toe}/H_{m0,deep}$. By combining the two parameters, the scatter is reduced significantly in Fig. 18(b). Therefore, in addition to describing the IG-wave generation mechanism, β_b also describes – to some extent – the relative magnitude of the IG waves.

Vegetated Cover

$H_{m0,IG,toe}$ [Fig. 19(a)] and $H_{m0,SS,toe}$ [Fig. 19(b)] both show negative exponential relationships with W_{veg}. The presence of vegetation, from $W_{veg} = 0$ m to $W_{veg} = 200$ m, notably reduces the wave heights at the dike toe; however, the effect is more significant for $H_{m0,IG,toe}$ than $H_{m0,SS,toe}$, with 60% and 46% reduction (on average), respectively. As a larger portion of the water column is under wave motion for longer-period (IG) waves, vegetation is able to more effectively reduce flow velocities. Therefore, submerged vegetation, also referred to as "canopies," attenuates IG-wave components more than do shorter-period (SS) components, as reported by Lowe et al. (2007) and Koftis et al. (2013).

Though the initial attenuation effect between nonvegetated ($W_{veg} = 0$ m) cover and some vegetation ($W_{veg} = 200$ m) is striking, a further increase in the width of vegetated cover does not significantly affect either $H_{m0,IG,toe}$ or $H_{m0,SS,toe}$ (Fig. 19). A similar response is seen in the average response of $\tilde{H}_{IG}$ to variations in W_{veg} ($\bar{\gamma}_v$), where the inclusion of 400 m of vegetation reduces $\bar{\gamma}_v$ by 40%, compared with the nonvegetated (reference) case, while a further increase in W_{veg} has only a minor effect (Fig. 20). This relationship may be described by

$$\bar{\gamma}_v = 0.94 \cdot e^{-W_{veg}/500} + 0.06 \cdot e^{W_{veg}/500} \tag{29}$$

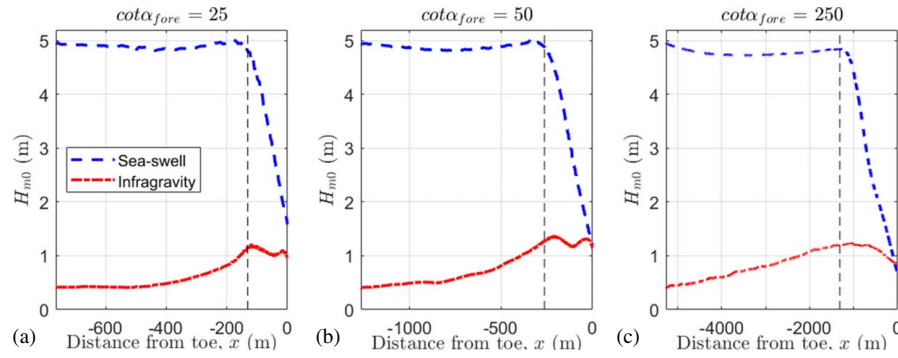where $\bar{\gamma}_v = 1$ corresponds to the reference case ($W_{veg} = 0$ m).

Fig. 16. Cross-shore profiles of $H_{m0,SS}$ and $H_{m0,IG}$ for: (a) cot $\alpha_{fore} = 25$; (b) cot $\alpha_{fore} = 50$; and (c) cot $\alpha_{fore} = 250$ ($H_{m0,deep} = 5$ m, $T_p = 11$ s, $\sigma = 0°$, $h_{toe} = 1$ m, $W_{veg} = 0$ m, and cot $\alpha_{dike} = \infty$). Vertical lines represent the mean breakpoint location, where $h_b = H_{m0}/0.8$.
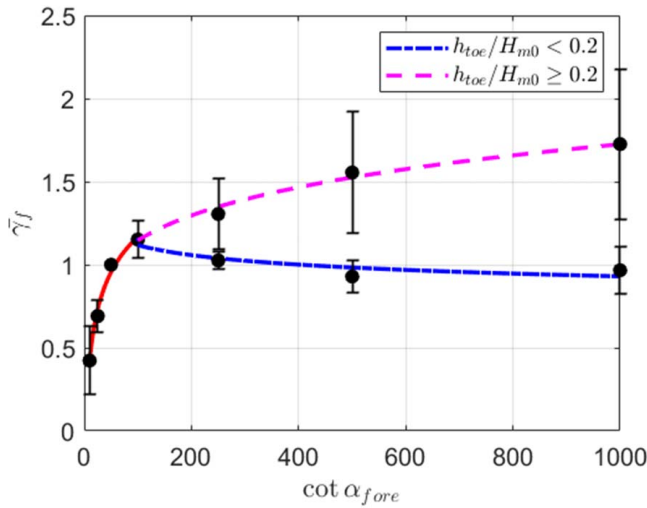

Fig. 17. Mean response of $\tilde{H}_{IG}$ to variations in cot α_{fore}, relative to the reference case (cot $\alpha_{fore} = 50$). Lines indicate the model fits [Eq. (28)]. Vertical error bars represent the standard deviation of each mean.

Bottom Friction

With respect to bottom friction, we assessed three general bed conditions: smooth concrete (wave flume, $n = 0.012$ s/m$^{1/3}$), mud ($n = 0.020$ s/m$^{1/3}$), and sand ($n = 0.03$ s/m$^{1/3}$). However, both $H_{m0,IG,toe}$ and $H_{m0,SS,toe}$ were found to be insensitive to n, experiencing only minor dissipation (<2%) with increasing n (not shown here). This finding agrees with previous studies that found that the dissipation of nearshore waves was governed by depth-induced wave-breaking (Henderson et al. 2006; Thomson et al. 2006; van Dongeren et al. 2007) and attenuation by vegetation (Baron-Hyppolite et al. 2019), but was insensitive to bottom friction. Thus, the influence of n on $\tilde{H}_{IG}$ can be considered negligible.

Dike Slope

The presence of a dike increases $H_{m0,IG,toe}$ by a factor of 2.1 (on average) compared with the no-dike (cot $\alpha_{dike} = \infty$) scenario [Fig. 21(a)]. This is due to the constructive inference of the incoming and reflected IG waves at the dike toe (as described in "Reflection of Infragravity Waves at the Dike"). This occurs for dike slopes as mild as cot $\alpha_{dike} = 10$, though a minor reduction in $H_{m0,IG,toe}$ is seen as the dike slope becomes milder (as cot α_{dike} increases). $H_{m0,SS,toe}$ experiences a similar increase in amplitude for cot $\alpha_{dike} = 2$ compared with the no-dike scenario [Fig. 21(b)]; however, this increase is only by a factor of 1.3 (on average).
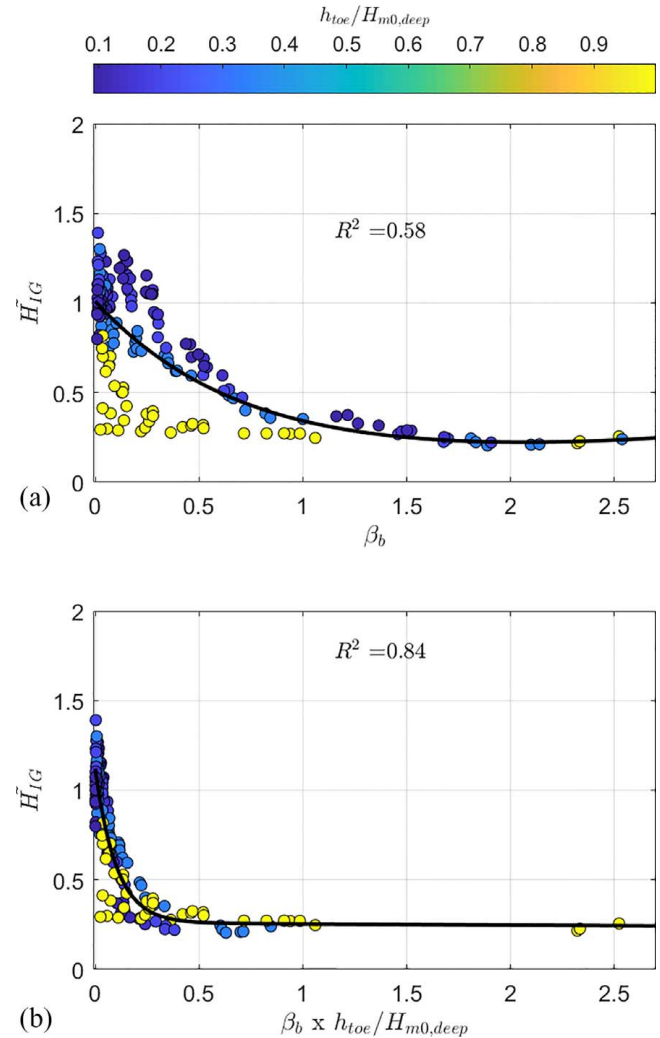

Fig. 18. Relationship between $\tilde{H}_{IG}$ and β_b for the seven different foreshore slopes simulated ($\sigma = 0°$, $h_{toe} = 1$ m, $W_{veg} = 0$ m, $n = 0.012$ s/m$^{1/3}$, and cot $\alpha_{dike} = \infty$). Colormap shows influence of relative water depth ($h_{toe}/H_{m0,deep}$).

This difference in amplification is due to the frequency-dependence of wave reflection – that is, lower-frequency (longer-period) waves experience greater reflection than those at higher frequencies. Furthermore, as the dike slope becomes milder (cot $\alpha_{dike} > 2$), the influence of the dike on $H_{m0,SS,toe}$ quickly becomes negligible [Fig. 21(b)].
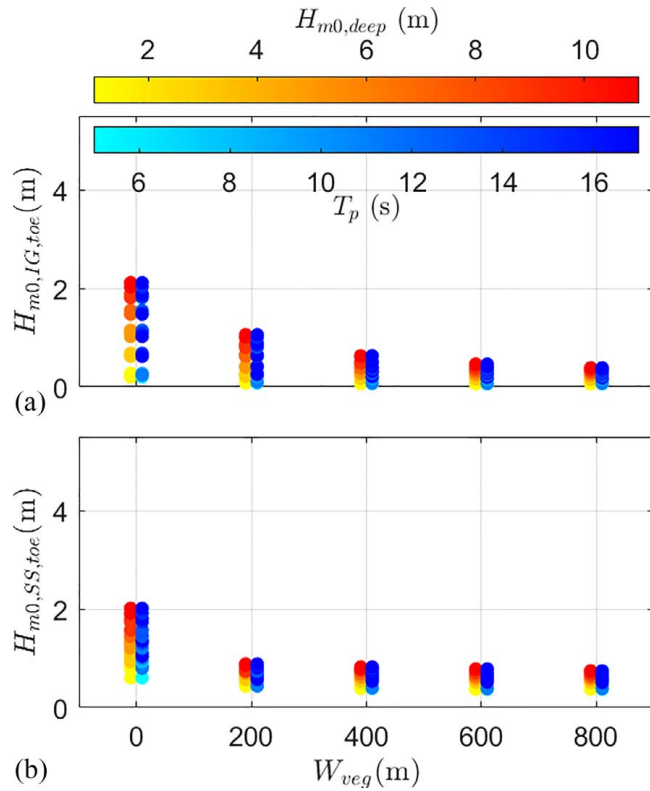
Fig. 19. Scatterplots of: (a) $H_{m0,IG,toe}$; and (b) $H_{m0,SS,toe}$ against W_{veg} ($\sigma = 0°$, $h_{toe} = 1$ m, cot $\alpha_{fore} = 50$, $n = 0.012$ s/m$^{1/3}$, and cot $\alpha_{dike} = \infty$). Each data point is represented by two markers with colormaps indicating the magnitude of $H_{m0,deep}$ (hot) and T_p (cold).
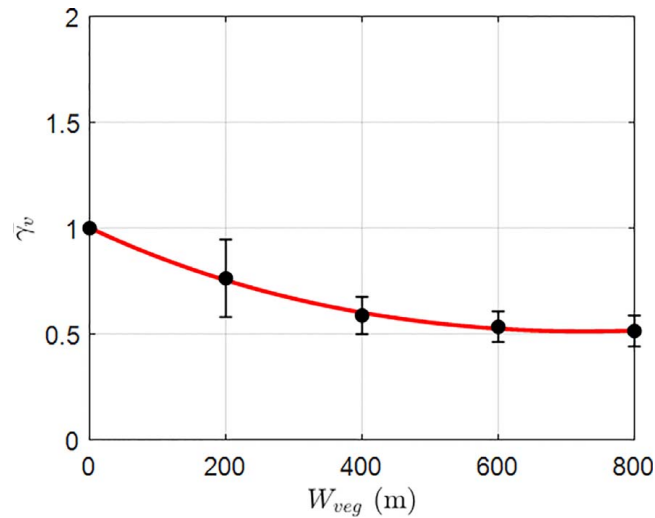

Fig. 21. Scatterplots of: (a) $H_{m0,IG,toe}$; and (b) $H_{m0,SS,toe}$ against cot α_{dike} ($\sigma = 0°$, $h_{toe} = 1$ m, cot $\alpha_{fore} = 50$, $W_{veg} = 0$ m, and $n = 0.012$ s/m$^{1/3}$). Each data point is represented by two markers with colormaps indicating the magnitude of $H_{m0,deep}$ (hot) and T_p (cold).

Fig. 20. Mean response of $\tilde{H}_{IG}$ to variations in W_{veg}, relative to the reference case ($W_{veg} = 0$ m). The line indicates the model fit [Eq. (29)]. Vertical error bars represent the standard deviation of each mean.

Fig. 22. Mean response of $\tilde{H}_{IG}$ to variations in cot α_{dike}, relative to the reference case (no-dike scenario). Line indicates the model fit [Eq. (30)]. Vertical error bars represent the standard deviation of each mean. Dashed line indicates the mean response obtained for the "no-dike" scenario.

As a result, the mean response of $\tilde{H}_{IG}$ to variations in cot α_{dike} ($\bar{\gamma}_d$) shows an initial positive relationship with cot α_{dike}, where it increases as the dike slope becomes milder, up to cot $\alpha_{dike} = 6$, but then decreases slightly for cot $\alpha_{dike} = 10$ (Fig. 22). The increased variation in $\bar{\gamma}_d$ for larger values of cot α_{dike} is due to the influence of T_p on wave reflection, where longer-period waves
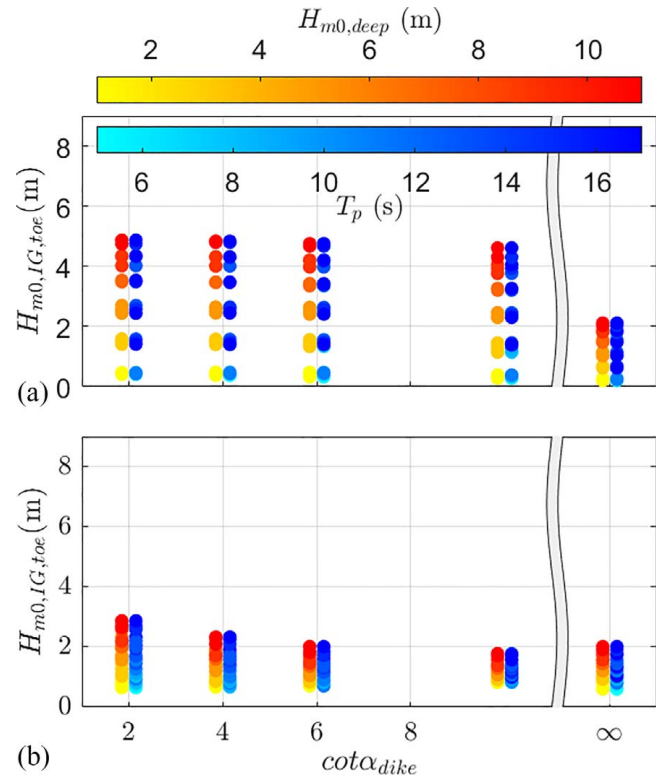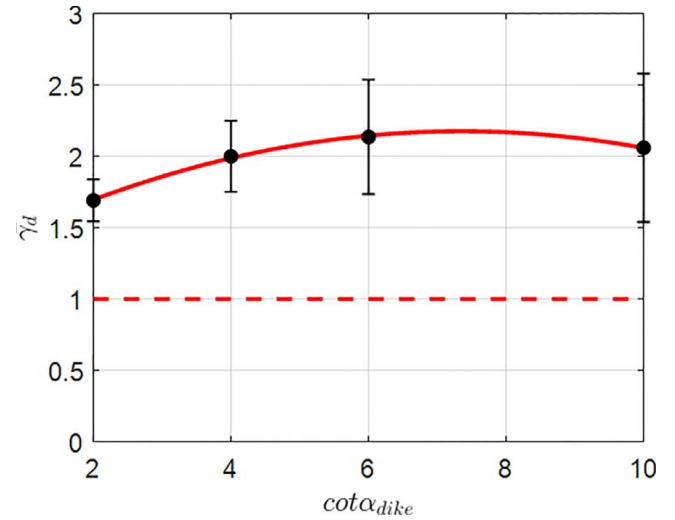
experience greater reflection at the dike, resulting in a larger $\tilde{H}_{IG}$ values.

$$\bar{\gamma}_d = 1.3 - 0.02 \cdot \cot\alpha_{dike}^2 + 0.24 \cdot \cot\alpha_{dike} \qquad (30)$$

where $\bar{\gamma}_d = 1$ corresponds to the reference case (no-dike scenario).

Predicting Nearshore Infragravity-Wave Dominance

By combining Eqs. (25) to (30), we may estimate $\tilde{H}_{IG}$ based on prior knowledge of offshore forcing ($H_{m0,deep}$ and σ), foreshore conditions (h_{toe}, cot α_{fore} and W_{veg}), and dike slope (cot α_{dike}) using:

$$\tilde{H}_{IG} = 0.36 \cdot H_{m0,deep}^{0.5} \cdot \bar{\gamma}_\sigma \cdot \bar{\gamma}_h \cdot \bar{\gamma}_f \cdot \bar{\gamma}_v \cdot \bar{\gamma}_d \qquad (31)$$

where subscripts σ, h, f, v, and d = initial water depth, directional spreading, foreshore slope, vegetated cover, bottom friction, and dike slope, respectively. To consider only incident wave conditions (no reflection), $\bar{\gamma}_d$ takes a value of 1. For conditions where $\tilde{H}_{IG} > 1$ (IG-wave dominance), the magnitude of nearshore IG waves exceeds that of SS waves and governs wave-driven processes, such as wave runup and overtopping; thus, under such conditions IG waves should not be neglected.

Fig. 23 presents the combined results of $\tilde{H}_{IG}$ for the physical modeling, observations obtained from 12 simulations and numerical modeling, 672 XBeach simulations. The proposed empirical model [Eq. (31)], developed using XBeach simulations alone, not only describes the entire dataset well ($R^2 = 0.94$) but also shows good agreement with the observations made during the physical experiment (SCI = 0.098 and Rel.bias = −0.07). The outliers shown in Fig. 23 are largely associated with simulations where nearshore conditions are not significantly influenced by the water depth ($h_{toe}/H_{m0,deep} = 1$) and $\tilde{H}_{IG}$ values are low (<0.5).

To verify the validity of OAT approach taken here, where the influence of each parameter was assessed independently, a test-case scenario, where multiple parameter values differed from the reference case, was simulated in XB-NH and the results compared with Eq. (31). This test case, with $H_{m0,deep} = 9$ m, $T_p = 15$ s, $\sigma = 0°$, $h_{toe} = 0.5$ m, cot $\alpha_{fore} = 100$, $W_{veg} = 200$ m, and cot $\alpha_{dike} = 6$, was also well represented by Eq. (31), shown by the blue marker in Fig. 23. This shows that the approach taken here does indeed take into account the interaction between environmental parameters.
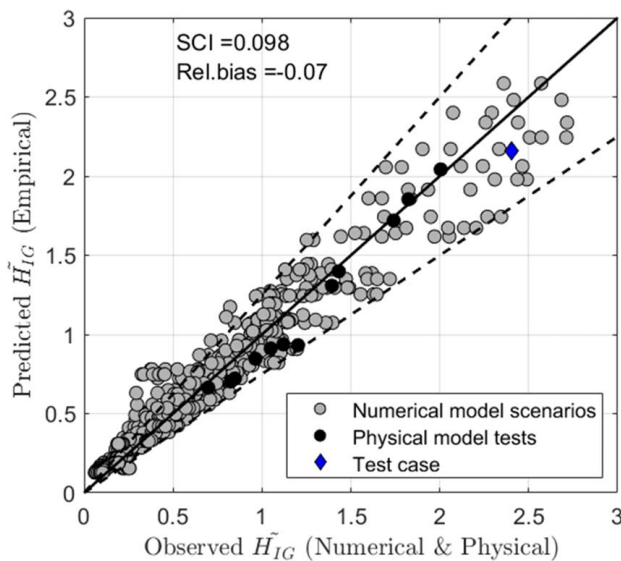

Fig. 23. Modeled [empirically, Eq. (31)] and observed comparison for the 12 physical model tests and 672 numerical model scenarios. Solid line indicates perfect agreement between empirical model and observations, dashed lines indicate ±20% error. Diamond marker indicates test case where multiple parameter values differed from the reference case.

Conclusions

A combination of physical and numerical modeling was applied to assess the range of offshore (H_{m0}, T_p, and σ), foreshore (h_{toe}, cot α_{fore}, W_{veg}, and n), and sea–dike (cot α_{dike}) conditions that promote the growth of nearshore IG waves. In particular, the exact conditions that result in the dominance of IG waves over SS waves ($\tilde{H}_{IG} > 1$) were identified. XBeach showed high skill in predicting $\bar{\eta}$, $H_{m0,SS}$, and $H_{m0,IG}$ when compared with physical observations, thereby laying a foundation of confidence in its performance. XBeach was then used to simulate a wide range of conditions, and thus to extend the analysis. Both the physical experiment and numerical simulations show that higher, directionally narrow-banded offshore waves; shallower water depths; milder foreshore slopes; reduced vegetated cover; and milder dike slopes give rise to IG-wave dominance. Both T_p and n were found to have minor influence on $\tilde{H}_{IG}$, for the reference slope (cot $\alpha_{fore} = 50$). However, this influence may increase for very mild slopes (cot $\alpha_{fore} \geq 500$), evident by the scatter displayed in Fig. 17.

XBeach simulations also reveal that, under shallow conditions, nearshore IG-wave energy is the result of both bound-wave shoaling and IG waves generated at the breakpoint. Likewise, reflection from the dike slope (as mild as cot $\alpha_{dike} = 10$) is shown to result in significant amplitude growth of IG waves at the dike toe. This is due to the interference of the incoming and the almost completely reflected signals that forms a standing wave with a node in the surf zone and an antinode at the shoreline.

The empirical model derived here [Eq. (31)], which captures the combined effect of the varied environmental parameters, would allow practitioners to quickly estimate the significance of IG waves at a given coast. This is particularly useful, as it indicates whether or not using a spectral wave model is sufficient (where $\tilde{H}_{IG}$ is minor), or whether a more cumbersome phase-resolving model is required (where $\tilde{H}_{IG}$ is significant). Furthermore, the empirical model may be combined with spectral wave models to extend their applicability to areas where the IG waves contribute significantly, as is often the case with shallow foreshore environments. Future work should verify the applicability of the proposed approach to field sites, considering the influence of alongshore variability and nonuniform foreshore morphologies, and investigate the influence of $\tilde{H}_{IG}$ on processes such as wave impact, runup, or overtopping. Finally, the approach adopted here independently assessed the influence of each environmental parameter; therefore, future work should also consider the dependencies, if any, among parameters.

Data Availability Statement

Some or all data, models, or code that support the findings of this study are available from the corresponding author upon reasonable request.

Acknowledgments

Ap van Dongeren and Ad Reniers for their review of key sections of this manuscript. Finally, we acknowledge Charles Feys for his contribution to the research.

Notation

The following symbols are used in this paper:

A = envelope of the sea and swell waves (m);
a = fitted coefficient in the prediction of $\tilde{H}_{IG}$ (m^{-1});
a_h = vegetation height (m);
b_v = vegetation stem diameter (m);
C_D = drag coefficient (−);
$C_{\eta\eta}$ = wave energy density (m^2/Hz);
c = wave speed (m/s);
c_f = bed friction factor (−);
c_g = wave-group velocity (m/s);
c_{in} = incoming wave speed (m/s);
c_{out} = outgoing wave speed (m/s);
F_D = drag force (N/m);
F_v = depth-averaged vegetation force (N);
f_{low} = mean frequency of the IG wave at breakpoint (Hz);
f_{node} = nodal frequency of standing wave (Hz);
f_p = peak frequency (Hz);
$\tilde{H}_{IG}$ = relative magnitude of the infragravity waves at the dike toe (−);
H_{m0} = local significant wave height (m);
$H_{m0,deep}$ = significant wave height offshore in deep water (m);
$H_{m0,IG}$ = significant wave height in the infragravity frequency band (m);
$H_{m0,IG,toe}$ = significant wave height in the infragravity frequency band, at the dike toe (m);
$H_{m0,SS}$ = significant wave height in the sea and swell frequency band (m);
$H_{m0,SS,toe}$ = significant wave height in the sea and swell frequency band, at the dike toe (m);
h = local water depth (m);
h_b = water depth at breakpoint (m);
h_{toe} = initial water depth at the dike toe (m);
k = wave number (rad/m);
L = local wavelength (m);
L_0 = wavelength in deep water (m);
m = mode of the dike–foreshore system (standing wave) (−);
N_v = vegetation stem density (stems/m^2);
n = manning roughness coefficient (s/m$^{1/3}$);
$\bar{q}$ = depth-averaged dynamic (nonhydrostatic) pressure normalized by the density (−);
Rel.bias = Relative Bias (−);
$R_{\eta A}$ = cross-correlation coefficient (−);
R^2 = coefficient of determination (−);
s = user-defined directional spreading factor (XBeach) (−);
s_0 = deep-water wave steepness (−);
SCI = scatter Index (−);
$T_{m-1,0}$ = spectral wave period (s);
T_p = peak wave period in deep water (s);
u = depth-averaged cross-shore velocity (m/s);
v_h = horizontal viscosity (m^2/s);
W_{veg} = width of vegetated cover (m);
x = cross-shore location (m);
x_b = cross-shore breakpoint location (m);
x_{dike} = cross-shore dike location (m);
α_{dike} = dike slope angle (°);
α_{fore} = foreshore slope angle (°);
β_b = normalized bed slope (−);
$\bar{\gamma}$ = Influence factor (−);
Δx = cross-shore grid spacing (m);
Δy = alongshore grid spacing (m);
η = surface elevation (m);
η^{IG} = low-pass filtered surface elevation (m);
$\bar{\eta}$ = mean water level relative to the dike toe (m);
η_{in}^{IG} = incoming low-pass filtered surface elevation (m);
η_{out}^{IG} = outgoing low-pass filtered surface elevation (m);
η^{SS} = high-pass filtered surface elevation (m);
ξ_0 = breaker index (Iribarren number) (−);
ρ = density of water (kg/m^3);
σ = directional spreading (°);
σ_A = standard deviation of the wave envelope time series (m);
σ_η = standard deviation of the low-pass filtered surface elevation time series (m);
ω = angular frequency (rad/s); and
Ω = ratio of breaking waves to water depth (−).

References

Altomare, C., T. Suzuki, X. Chen, T. Verwaest, and A. Kortenhaus. 2016. "Wave overtopping of sea dikes with very shallow foreshores." *Coastal Eng.* 116: 236–257. https://doi.org/10.1016/j.coastaleng.2016.07.002.

Baldock, T. E. 2006. "Long wave generation by the shoaling and breaking of transient wave groups on a beach." *Proc. R. Soc. London, Ser. A* 462 (2070): 1853–1876. https://doi.org/10.1098/rspa.2005.1642.

Baldock, T. E. 2012. "Dissipation of incident forced long waves in the surf zone—implications for the concept of "bound" wave release at short wave breaking." *Coastal Eng.* 60: 276–285. https://doi.org/10.1016/j.coastaleng.2011.11.002.

Baldock, T. E., and D. A. Huntley. 2002. "Long-wave forcing by the breaking of random gravity waves on a beach." *Proc. R. Soc. London, Ser. A* 458 (2025): 2177–2201. https://doi.org/10.1098/rspa.2002.0962.

Baldock, T. E., D. A. Huntley, P. A. D. Bird, T. O'Hare, and G. N. Bullock. 2000. "Breakpoint generated surf beat induced by bichromatic wave groups." *Coastal Eng.* 39 (2–4): 213–242. https://doi.org/10.1016/S0378-3839(99)00061-7.

Baron-Hyppolite, C., C. Lashley, J. Garzon, T. Miesse, C. Ferreira, and J. Bricker. 2019. "Comparison of implicit and explicit vegetation representations in SWAN hindcasting wave dissipation by coastal wetlands in Chesapeake Bay." *Geosciences* 9 (1): 8. https://doi.org/10.3390/geosciences9010008.

Battjes, J. A., H. J. Bakkenes, T. T. Janssen, and A. R. van Dongeren. 2004. "Shoaling of subharmonic gravity waves." *J. Geophys. Res.* 109 (C2): C02009. https://doi.org/10.1029/2003JC001863.

Baumann, J., E. Chaumillon, X. Bertin, J. L. Schneider, B. Guillot, and M. Schmutz. 2017. "Importance of infragravity waves for the generation of washover deposits." *Mar. Geol.* 391: 20–35. https://doi.org/10.1016/j.margeo.2017.07.013.

Booij, N., R. C. Ris, and L. H. Holthuijsen. 1999. "A third-generation wave model for coastal regions—1. Model description and validation." *J. Geophys. Res.* 104 (C4): 7649–7666. https://doi.org/10.1029/98JC02622.

Buckley, M. L., R. J. Lowe, J. E. Hansen, A. R. van Dongeren, and C. D. Storlazzi. 2018. "Mechanisms of wave-driven water level variability on reef-fringed coastlines." *J. Geophys. Res.* 123 (5): 3811–3831. https://doi.org/10.1029/2018JC013933.

Contardo, S., and G. Symonds. 2013. "Infragravity response to variable wave forcing in the nearshore." *J. Geophys. Res.* 118 (12): 7095–7106. https://doi.org/10.1002/2013JC009430.

Cox, N., L. M. Dunkin, and J. L. Irish. 2013. "An empirical model for infragravity swash on barred beaches." *Coastal Eng.* 81: 44–50. https://doi.org/10.1016/j.coastaleng.2013.06.008.

Dalrymple, R. A., J. T. Kirby, and P. A. Hwang. 1984. "Wave diffraction due to areas of energy dissipation." *J. Waterw. Port Coastal Ocean*

Eng. 110 (1): 67–79. https://doi.org/10.1061/(ASCE)0733-950X(1984)110:1(67).

de Bakker, A. T. M., M. F. S. Tissier, and B. G. Ruessink. 2014. "Shoreline dissipation of infragravity waves." *Cont. Shelf Res.* 72: 73–82. https://doi.org/10.1016/j.csr.2013.11.013.

Gomes da Silva, P., R. Medina, M. González, and R. Garnier. 2018. "Infragravity swash parameterization on beaches: The role of the profile shape and the morphodynamic beach state." *Coastal Eng.* 136: 41–55. https://doi.org/10.1016/j.coastaleng.2018.02.002.

Guza, R. T., and E. B. Thornton. 1982. "Swash oscillations on a natural beach." *J. Geophys. Res.* 87 (C1): 483–491. https://doi.org/10.1029/JC087iC01p00483.

Guza, R. T, E. B. Thornton, and R. Holman. 1984. "Swash on steep and shallow beaches." In *Proc., 19th Int. Conf. on Coastal Engineering*, edited by B. L. Edge, 708–723. Reston, VA: ASCE.

Henderson, S. M., and A. J. Bowen. 2002. "Observations of surf beat forcing and dissipation." *J. Geophys. Res.* 107 (C11): 14-11–14-10. https://doi.org/10.1029/2000JC000498.

Henderson, S. M., R. T. Guza, S. Elgar, T. H. C. Herbers, and A. J. Bowen. 2006. "Nonlinear generation and loss of infragravity wave energy." *J. Geophys. Res.* 111 (C12): C12007. https://doi.org/10.1029/2006JC003539.

Hofland, B., X. Chen, C. Altomare, and P. Oosterlo. 2017. "Prediction formula for the spectral wave period $T_{m-1,0}$ on mildly sloping shallow foreshores." *Coastal Eng.* 123: 21–28. https://doi.org/10.1016/j.coastaleng.2017.02.005.

Holman, R. A., and A. H. Sallenger. 1985. "Setup and swash on a natural beach." *J. Geophys. Res.* 90 (C1): 945–953. https://doi.org/10.1029/JC090iC01p00945.

Inch, K., M. Davidson, G. Masselink, and P. Russell. 2017. "Observations of nearshore infragravity wave dynamics under high energy swell and wind-wave conditions." *Cont. Shelf Res.* 138: 19–31. https://doi.org/10.1016/j.csr.2017.02.010.

Janssen, T. T., J. A. Battjes, and A. R. van Dongeren. 2003. "Long waves induced by short-wave groups over a sloping bottom." *J. Geophys. Res.* 108 (C8): 3252. https://doi.org/10.1029/2002JC001515.

Klopman, G., and J. W. van der Meer. 1999. "Random wave measurements in front of reflective structures." *J. Waterw. Port Coastal Ocean Eng.* 125 (1): 39–45. https://doi.org/10.1061/(ASCE)0733-950X(1999)125:1(39).

Koftis, T., P. Prinos, and V. Stratigaki. 2013. "Wave damping over artificial Posidonia oceanica meadow: A large-scale experimental study." *Coastal Eng.* 73: 71–83. https://doi.org/10.1016/j.coastaleng.2012.10.007.

Lara, J. L., A. Ruju, and I. J. Losada. 2011. "Reynolds averaged Navier–Stokes modeling of long waves induced by a transient wave group on a beach." *Proc. R. Soc. London, Ser. A* 467 (2129): 1215–1242. https://doi.org/10.1098/rspa.2010.0331.

Lashley, C. H., X. Bertin, D. Roelvink, and G. Arnaud. 2019a. "Contribution of infragravity waves to run-up and overwash in the pertuis Breton embayment (France)." *J. Mar. Sci. Eng.* 7 (7): 205. https://doi.org/10.3390/jmse7070205.

Lashley, C. H., J. D. Bricker, J. van der Meer, C. Altomare, and T. Suzuki. 2019b. "Infragravity-wave dominance at Sea-dikes fronted by very and extremely shallow foreshores." In *Proc., 29th Int. Ocean and Polar Engineering Conf.*, 1–7. Mountain View, CA: ISOPE.

Lashley, C. H., D. Roelvink, A. van Dongeren, M. L. Buckley, and R. J. Lowe. 2018. "Nonhydrostatic and surfbeat model predictions of extreme wave run-up in fringing reef environments." *Coastal Eng.* 137: 11–27. https://doi.org/10.1016/j.coastaleng.2018.03.007.

List, J. H. 1992. "A model for the generation of two-dimensional surf beat." *J. Geophys. Res.* 97 (C4): 5623–5635. https://doi.org/10.1029/91JC03147.

Longuet-Higgins, M. S., and R. W. Stewart. 1962. "Radiation stress and mass transport in gravity waves, with application to "surf beats"." *J. Fluid Mech.* 13 (4): 481–504. https://doi.org/10.1017/S0022112062000877.

Lowe, R. J., J. L. Falter, J. R. Koseff, S. G. Monismith, and M. J. Atkinson. 2007. "Spectral wave flow attenuation within submerged canopies: Implications for wave energy dissipation." *J. Geophys. Res.* 112 (C5): C05018. https://doi.org/10.1029/2006JC003605.

Mase, H., T. Tamada, T. Yasuda, T. S. Hedges, and M. T. Reis. 2013. "Wave runup and overtopping at seawalls built on land and in very shallow water." *J. Waterw. Port Coastal Ocean Eng.* 139 (5): 346–357. https://doi.org/10.1061/(ASCE)WW.1943-5460.0000199.

Masselink, G. 1995. "Group bound long waves as a source of infragravity energy in the surf zone." *Cont. Shelf Res.* 15 (13): 1525–1547. https://doi.org/10.1016/0278-4343(95)00037-2.

McCall, R. T., G. Masselink, T. G. Poate, J. A. Roelvink, and L. P. Almeida. 2015. "Modeling the morphodynamics of gravel beaches during storms with XBeach-G." *Coastal Eng.* 103: 52–66. https://doi.org/10.1016/j.coastaleng.2015.06.002.

Nwogu, O., and Z. Demirbilek. 2010. "Infragravity wave motions and runup over shallow fringing reefs." *J. Waterw. Port Coastal Ocean Eng.* 136 (6): 295–305. https://doi.org/10.1061/(ASCE)WW.1943-5460.0000050.

Okihiro, M., R. T. Guza, and R. J. Seymour. 1993. "Excitation of seiche observed in a small harbor." *J. Geophys. Res.* 98 (C10): 18201–18211. https://doi.org/10.1029/93JC01760.

Passarella, M., E. B. Goldstein, S. De Muro, and G. Coco. 2018. "The use of genetic programming to develop a predictor of swash excursion on sandy beaches." *Nat. Hazards Earth Syst. Sci.* 18 (2): 599–611. https://doi.org/10.5194/nhess-18-599-2018.

Pearson, S. G., C. D. Storlazzi, A. R. van Dongeren, M. F. S. Tissier, and A. J. H. M. Reniers. 2017. "A Bayesian-based system to assess wave-driven flooding hazards on coral reef-lined coasts." *J. Geophys. Res.* 122 (12): 10099–10117. https://doi.org/10.1002/2017JC013204.

Percival, D. B., and A. T. Walden. 1993. *Spectral analysis for physical applications*. Cambridge: Cambridge University Press. https://doi.org/10.1017/CBO9780511622762.

Pomeroy, A., R. Lowe, G. Symonds, A. van Dongeren, and C. Moore. 2012. "The dynamics of infragravity wave transformation over a fringing reef." *J. Geophys. Res.* 117 (C11): C11022. https://doi.org/10.1029/2012JC008310.

Power, H. E., M. G. Hughes, T. Aagaard, and T. E. Baldock. 2010. "Nearshore wave height variation in unsaturated surf." *J. Geophys. Res.* 115 (C8): C08030. https://doi.org/10.1029/2009JC005758.

Roeber, V., and J. D. Bricker. 2015. "Destructive tsunami-like wave generated by surf beat over a coral reef during Typhoon Haiyan." *Nat. Commun.* 6 (1): 7854. https://doi.org/10.1038/ncomms8854.

Roelvink, D., R. McCall, S. Mehvar, K. Nederhoff, and A. Dastgheib. 2018. "Improving predictions of swash dynamics in XBeach: The role of groupiness and incident-band runup." *Coastal Eng.* 134: 103–123. https://doi.org/10.1016/j.coastaleng.2017.07.004.

Roelvink, D., A. Reniers, A. van Dongeren, J. van Thiel de Vries, R. McCall, and J. Lescinski. 2009. "Modeling storm impacts on beaches, dunes and barrier islands." *Coastal Eng.* 56 (11–12): 1133–1152. https://doi.org/10.1016/j.coastaleng.2009.08.006.

Roelvink, D., A. van Dongeren, R. McCall, B. Hoonhout, A. van Rooijen, P. van Geer, L. De Vet, K. Nederhoff, and E. Quataert. 2015. *XBeach technical reference: Kingsday release*. Technical Rep.. Delft, Netherlands: Deltares.

Roelvink, J. A., and M. J. F. Stive. 1989. "Bar-generating cross-shore flow mechanisms on a beach." *J. Geophys. Res.* 94 (C4): 4785–4800. https://doi.org/10.1029/JC094iC04p04785.

Ruessink, B. G., M. G. Kleinhans, and P. G. L. van den Beukel. 1998. "Observations of swash under highly dissipative conditions." *J. Geophys. Res.* 103 (C2): 3111–3118. https://doi.org/10.1029/97JC02791.

Ruggiero, P., R. A. Holman, and R. A. Beach. 2004. "Wave run-up on a high-energy dissipative beach." *J. Geophys. Res.* 109 (C6): C06025. https://doi.org/10.1029/2003JC002160.

Sheremet, A., R. Guza, S. Elgar, and T. Herbers. 2002. "Observations of nearshore infragravity waves: Seaward and shoreward propagating components." *J. Geophys. Res.* 107 (C8): 3095. https://doi.org/10.1029/2001JC000970.

Sheremet, A., T. Staples, F. Ardhuin, S. Suanez, and B. Fichaut. 2014. "Observations of large infragravity wave runup at Banneg Island, France." *Geophys. Res. Lett.* 41 (3): 976–982. https://doi.org/10.1002/2013GL058880.

Shimozono, T., Y. Tajima, A. B. Kennedy, H. Nobuoka, J. Sasaki, and S. Sato. 2015. "Combined infragravity wave and sea-swell runup over

fringing reefs by super typhoon Haiyan." *J. Geophys. Res.* 120 (6): 4463–4486. https://doi.org/10.1002/2015JC010760.

Smagorinsky, J. 1963. "General circulation experiments with the primitive equations." *Mon. Weather Rev.* 91 (3): 99–164. https://doi.org/10.1175/1520-0493(1963)091<0099:GCEWTP>2.3.CO;2.

Smit, P., G. Stelling, J. Roelvink, J. van Thiel de Vries, R. McCall, A. van Dongeren, C. Zwinkels, and R. Jacobs. 2010. *XBeach: Non-hydrostatic model: Validation, verification and model description*. Delft, Netherlands: Delft Univ. of Technology.

Smith, J. M., A. R. Sherlock, and D. T. Resio. 2001. *STWAE: Steady-state spectral wave model user's manual for STWAVE, version 3.0.* Washington, DC: U.S. Army Corps of Engineers.

Stockdon, H. F., R. A. Holman, P. A. Howd, and A. H. Sallenger. 2006. "Empirical parameterization of setup, swash, and runup." *Coastal Eng.* 53 (7): 573–588. https://doi.org/10.1016/j.coastaleng.2005.12.005.

Suzuki, T., C. Altomare, W. Veale, T. Verwaest, K. Trouw, P. Troch, and M. Zijlema. 2017. "Efficient and robust wave overtopping estimation for impermeable coastal structures in shallow foreshores using SWASH." *Coastal Eng.* 122: 108–123. https://doi.org/10.1016/j.coastaleng.2017.01.009.

Suzuki, T., Z. Hu, K. Kumada, L. K. Phan, and M. Zijlema. 2019. "Non-hydrostatic modeling of drag, inertia and porous effects in wave propagation over dense vegetation fields." *Coastal Eng.* 149: 49–64. https://doi.org/10.1016/j.coastaleng.2019.03.011.

Suzuki, T., M. Zijlema, B. Burger, M. C. Meijer, and S. Narayan. 2012. "Wave dissipation by vegetation with layer schematization in SWAN." *Coastal Eng.* 59 (1): 64–71. https://doi.org/10.1016/j.coastaleng.2011.07.006.

Symonds, G., D. A. Huntley, and A. J. Bowen. 1982. "Two-dimensional surf beat: Long wave generation by a time-varying breakpoint." *J. Geophys. Res.* 87 (C1): 492–498. https://doi.org/10.1029/JC087iC01p00492.

Thomson, J., S. Elgar, B. Raubenheimer, T. H. C. Herbers, and R. T. Guza. 2006. "Tidal modulation of infragravity waves via nonlinear energy losses in the surfzone." *Geophys. Res. Lett.* 33 (5): L05601. https://doi.org/10.1029/2005GL025514.

van der Meer, J., N. Allsop, T. Bruce, J. De Rouck, A. Kortenhaus, T. Pullen, H. Schuttrumpf, P. Troch, and B. Zanuttigh. 2018. EurOtop 2018: Manual on wave overtopping of sea defences and related structures. An overtopping manual largely based on European research, but for worldwide application. https://www.overtopping-manual.com.

van Dongeren, A., J. Battjes, T. Janssen, J. van Noorloos, K. Steenhauer, G. Steenbergen, and A. Reniers. 2007. "Shoaling and shoreline dissipation of low-frequency waves." *J. Geophys. Res.* 112 (C2): C02011. https://doi.org/10.1029/2006JC003701.

van Dongeren, A., A. Reniers, J. Battjes, and I. Svendsen. 2003. "Numerical modeling of infragravity wave response during DELILAH." *J. Geophys. Res.* 108 (C9): 3288. https://doi.org/10.1029/2002JC001332.

van Dongeren, A. R., and I. A. Svendsen. 1997. *Quasi 3-D modeling of nearshore hydrodynamics*. Newark, DE: Center for Applied Coastal Research, Univ. of Delaware.

van Gent, M. R. A. 2001. "Wave runup on dikes with shallow foreshores." *J. Waterw. Port Coastal Ocean Eng.* 127 (5): 254–262. https://doi.org/10.1061/(ASCE)0733-950X(2001)127:5(254).

van Rooijen, A., R. McCall, J. van Thiel de Vries, A. van Dongeren, A. Reniers, and J. Roelvink. 2016. "Modeling the effect of wave-vegetation interaction on wave setup." *J. Geophys. Res.* 121 (6): 4341–4359. https://doi.org/10.1002/2015JC011392.

Vuik, V., S. N. Jonkman, B. W. Borsje, and T. Suzuki. 2016. "Nature-based flood protection: The efficiency of vegetated foreshores for reducing wave loads on coastal dikes." *Coastal Eng.* 116: 42–56. https://doi.org/10.1016/j.coastaleng.2016.06.001.

Yao, Y., Z. Huang, S. G. Monismith, and E. Y. M. Lo. 2013. "Characteristics of monochromatic waves breaking over fringing reefs." *J. Coastal Res.* 29 (1): 94–104. https://doi.org/10.2112/JCOASTRES-D-12-00021.1.